HHS Public Access

Author manuscript

Science. Author manuscript; available in PMC 2024 August 06.

Published in final edited form as:

Science. 2024 June 07; 384(6700): eadk0850. doi:10.1126/science.adk0850.

Determining the ERK-regulated phosphoproteome driving KRAS-mutant cancer

Jennifer E. Klomp[1], **J. Nathaniel Diehl**[3], **Jeffrey A. Klomp**[1,2], **A. Cole Edwards**[4], **Runying Yang**[1], **Alexis J. Morales**[1], **Khalilah E. Taylor**[1], **Kristina Drizyte-Miller**[1], **Kirsten L. Bryant**[1,2], **Antje Schaefer**[1,2], **Jared L. Johnson**[5,6], **Emily M. Huntsman**[7,8], **Tomer M. Yaron**[7,8,9], **Mariaelena Pierobon**[10], **Elisa Baldelli**[10], **Alex W. Prevatte**[11], **Natalie K. Barker**[11], **Laura E. Herring**[11], **Emanuel F. Petricoin III**[10], **Lee M. Graves**[1,2,11], **Lewis C. Cantley**[5,6], **Adrienne D. Cox**[1,2,4,12], **Channing J. Der**[1,2,3,4,*], **Clint A. Stalnecker**[1,2,*]

[1]Lineberger Comprehensive Cancer Center; University of North Carolina at Chapel Hill, Chapel Hill, NC 27599, USA.

[2]Department of Pharmacology, University of North Carolina at Chapel Hill, Chapel Hill, NC 27599, USA.

[3]Curriculum in Genetics and Molecular Biology, University of North Carolina at Chapel Hill, Chapel Hill, NC 27599, USA.

[4]Cell Biology and Physiology Curriculum, University of North Carolina at Chapel Hill, Chapel Hill, NC 27599, USA.

[5]Department of Cell Biology, Harvard Medical School, Boston, MA 02115, USA.

[6]Dana-Farber Cancer Institute, Harvard Medical School, Boston, MA 02115, USA.

[7]Meyer Cancer Center, Weill Cornell Medicine; New York, NY 10065, USA.

[8]Englander Institute for Precision Medicine, Institute for Computational Biomedicine, Weill Cornell Medicine, New York, NY 10021, USA.

[9]Columbia University Vagelos College of Physicians and Surgeons, New York, NY 10032, USA.

[10]School of Systems Biology, George Mason University, Fairfax, VA 22030, USA.

[*]Corresponding authors: cjder@med.unc.edu (C.J.D.), clints@email.unc.edu (C.A.S.).

Author contributions

Project conceptions: C.J.D., J.N.D. and C.A.S.

Designed experiments and analyzed data: J.N.D., J.E.K., C.J.D. and C.A.S.

Performed experiments: J.E.K., J.N.D., A.C.E., R.Y., A.J.M., K.E.T., K.D.M., K.L.B., A.S., M.P., E.B., A.W.P., N.K.B., L.E.H., and C.A.S.

Contributed data and/or participated in discussions: J.E.K., J.N.D., J.A.K., J.L.J., E.M.H., T.M.Y., L.E.H., E.F.P., L.M.G., L.C.C. and A.D.C.

Computational analyses: led by C.A.S., assisted by J.A.K., E.M.H., and T.M.Y.

Manuscript writing J.E.K., J.A.K., A.D.C., C.J.D., and C.A.S.

All authors reviewed and approved the manuscript

List of Supplementary Materials:

Fig. S1–S6

Table S1–S5

Data S1–S8

MDAR Reproducibility Checklist

[11]UNC Michael Hooker Proteomics Center, University of North Carolina at Chapel Hill, Chapel Hill, NC 27599, USA.

[12]Department of Radiation Oncology, University of North Carolina at Chapel Hill; Chapel Hill, NC 27599, USA

Abstract

To delineate the mechanisms by which the ERK1 and ERK2 mitogen-activated protein kinases support mutant KRAS-driven cancer growth, we determined the ERK-dependent phosphoproteome in KRAS-mutant pancreatic cancer. We determined that ERK1 and ERK2 share near-identical signaling and transforming outputs and that the KRAS-regulated phosphoproteome is driven nearly completely by ERK. We identified 4,666 ERK-dependent phosphosites on 2,123 proteins, of which 79% and 66%, respectively, were not previously associated with ERK, substantially expanding the depth and breadth of ERK-dependent phosphorylation events and revealing a considerably more complex function for ERK in cancer. We established that ERK controls a highly dynamic and complex phosphoproteome that converges on cyclin-dependent kinase regulation and RHO GTPase function. Our findings establish the most comprehensive molecular portrait and mechanisms by which ERK drives KRAS-dependent pancreatic cancer growth.

ONE-SENTENCE SUMMARY

The ERK-regulated phosphoproteome dynamically controls diverse cellular processes to drive KRAS-mutant-dependent pancreatic cancer growth.

Mutational activation of the *KRAS* oncogene is a major genetic driver of pancreatic ductal adenocarcinoma (PDAC) growth (1). The best-studied immediate KRAS effectors are the RAF serine/threonine kinases (ARAF, BRAF and RAF1/CRAF) (2–4). Active RAS-GTP binds to and promotes activation of RAF kinase activity. Activated RAF then phosphorylates and activates the highly related MEK1 and MEK2 dual-specificity protein kinases, which in turn phosphorylate and activate the highly related ERK1 and ERK2 serine/threonine kinases (5, 6).

Whereas RAF and MEK exhibit highly restricted substrate utilization, ERK substrate utilization is broad and diverse (5, 6). How ERK drives KRAS-mutant cancer growth remains poorly understood. In our recent determination of the KRAS- and ERK-dependent transcriptome in KRAS-mutant cancers (7), we found that the transcriptional output of KRAS is largely driven by ERK. We also determined that reactivation of ERK by MEK alone was sufficient to drive near-complete resistance to $KRAS^{G12C}$ and $KRAS^{G12D}$ mutant-selective inhibitors. These findings, as well as the significant divergence of our KRAS-mutant dependent transcriptome from the Molecular Signatures Database Hallmark KRAS signature (8), provided the rationale for our current study to determine the ERK-dependent phosphoproteome. We focused on pathologic ERK signaling driven by endogenous oncogenic *KRAS* in the most KRAS-addicted cancer, pancreatic ductal adenocarcinoma (PDAC), that has a 95% *KRAS* mutation frequency.

Results

ERK1 and ERK2 support KRAS-dependent growth

We recently determined that activated MEK1 but not AKT1 is sufficient to render PDAC cells insensitive to direct pharmacologic inhibition of mutant KRAS (7). Unlike MEK1, activating mutations in ERK are not found in cancer, likely because single point mutations alone are not sufficient for full activation and therefore act as relatively weak oncogenes (9). To determine the degree to which ERK activation is sufficient to support KRAS-driven PDAC growth, we generated constitutively activated variants of ERK1 and ERK2 (83% identity) by combining previously described point mutations that each alone increase ERK1/2 activity (9–11) (Fig. 1A). Transient doxycycline (Dox)-inducible expression of each ERK1 mutant in the $KRAS^{G12D}$-mutant PDAC cell line Pa16C (fig. S1A) demonstrated that the double mutant $ERK1^{R84S/S170D}$ (designated $ERK1^{SD}$) most strongly induced phosphorylation of the ERK substrate FRA1 (pFRA1) (fig. S1B). We selected this and the analogous mutant of ERK2 (R67S/S153D; $ERK2^{SD}$) for further analyses (Fig. 1A).

We established Dox-inducible expression of MYC epitope-tagged $ERK1^{SD}$ or $ERK2^{SD}$ in $KRAS^{G12C}$ (MIA PaCa-2 and UM53) or $KRAS^{G12D}$ (Pa16C) mutant PDAC cell lines (fig. S1A). Dox treatment stimulated $ERK1/2^{SD}$ expression at levels comparable to endogenous ERK without significantly altering phosphorylation of the ERK substrate RSK (pRSK) or expression of MYC, which is stabilized by direct ERK phosphorylation (12) (Fig. 1B and fig. S1C). We then evaluated whether expression of ERK^{SD} mutants would impact the ability of pharmacologic inhibitors targeting different nodes of the KRAS-ERK MAPK cascade to inhibit PDAC growth.

As expected, $ERK1/2^{SD}$-expressing cells were resistant to the MEK1/2-selective inhibitor trametinib (MEKi) (fig. S1D) but retained sensitivity to the ERK1/2-selective inhibitor SCH772984 (ERKi) (Fig. 1C). Thus, activated $ERK1/2^{SD}$-expressing cells retained ERK-dependent growth upon MEK inhibition. As anticipated, treatment with either a $KRAS^{G12C}$-selective inhibitor (MRTX1257, analog of adagrasib/MRTX849; G12Ci) (13) or the clinical candidate $KRAS^{G12D}$- (MRTX1133; G12Di) (14) selective inhibitor reduced MYC and pRSK levels in control cells, which was significantly rescued by $ERK1/2^{SD}$ expression (Fig. 1B and fig. S1C). Unexpectedly, given the role of multiple other effectors in supporting KRAS driver function in PDAC (15), we observed that activated ERK alone was able to cause complete to near-complete resistance to growth inhibition (Fig. 1C). However, this result is consistent with genetically-engineered mouse models where pancreas expression of mutationally activated $Braf^{V600E}$ but not $Pik3ca^{H1047R}$ phenocopied mutant $Kras^{G12D}$ to drive development of metastatic PDAC (16). This result is also consistent with the ~200-fold greater affinity of RAS-GTP for RAF versus PI3Kα (17, 18) and with a systemwide proteomic assessment of RAS association with 56 effectors showing that RAS-RAF is the predominant RAS-effector complex (19).

An unresolved issue is whether the highly related ERK1 and ERK2 isoforms (83% identity) possess distinct or redundant biological functions (20). Our finding that either activated ERK1 or ERK2 alone can drive resistance to KRAS inhibition (Fig. 1C) supports their overlapping functions in promoting KRAS-dependent PDAC growth. To further address this

question, we performed acute siRNA-mediated suppression of either *MAPK3* (ERK1) or *MAPK1* (ERK2) alone or concurrently and evaluated the consequences for signaling and growth in four $KRAS^{G12D}$-mutant and two $KRAS^{G12C}$-mutant PDAC cell lines (fig. S1, E and F). We also included *KRAS* suppression, to assess the role of ERK in KRAS function.

We determined that siRNA suppression of either *MAPK3*/ERK1 or *MAPK1*/ERK2 alone strongly impaired PDAC growth, comparable to suppression of *KRAS* itself. While this result would be consistent with distinct functions of ERK1 and ERK2, it is also consistent with the prevailing evidence for a threshold requirement for the total combined level of ERK1 and ERK2 rather than for isoform-selective functions (20).

To determine if ERK1 and ERK2 regulate distinct signaling activities, we performed reverse phase protein array (RPPA) profiling of 147 established signaling proteins and phosphorylation events in six $KRAS^{G12C/D}$-mutant PDAC cell lines (fig. S1, A and G, and data S1). Spearman correlations of the signaling changes observed upon ERK1 or ERK2 suppression were high, indicating that the signaling changes were nearly identical, supporting the conclusion that their functions are redundant rather than distinct (Fig. 1D, and fig. S1, H and I). Providing further support for redundant functions of ERK1 and ERK2, we found that ectopic expression of $ERK1^{SD}$ or $ERK2^{SD}$ attenuated nearly all G12Di-induced transcriptional changes (by 92% and 83%, respectively) (Fig. 1, E and F). Finally, the signaling changes caused by acute siRNA suppression of *KRAS* and *ERK* were similar, differing primarily in their relative intensities (fig. S1I). Together, these observations support redundant signaling outputs of ERK1 and ERK2 in supporting KRAS-dependent growth.

ERK-dependent phosphoproteome in KRAS-mutant PDAC

Recently, Ünal *et al.* created a compendium of ERK substrates (21) by collating the data from an earlier compilation of ERK substrates (22) together with 12 mass spectrometry-based phosphoproteomic analyses and the PhosphoSitePlus (PSP) database. The resulting Compendium was comprised of 2,507 ERK dependent phosphosites on 1,310 proteins, of which 26% were defined as direct ERK phosphosites. This ERK Compendium of direct/indirect ERK substrates (21) did not include any data derived from KRAS-mutant pancreatic cancer (fig. S2A). Therefore, we determined the ERK-dependent phosphoproteome in KRAS-mutant PDAC cell lines. Further, whereas most previous studies evaluated ERK substrates under conditions of transient ERK activation such as EGF stimulation, our analysis focused on ERK substrates under conditions of pathologic ERK activation driven by mutant KRAS.

We utilized the ATP-competitive and allosteric ERKi SCH772984, shown by *in vitro* studies with purified recombinant protein kinases to be highly selective for ERK1/2. To assess its selectivity in PDAC cell cultures, we utilized the well-established multiplexed kinase inhibitor beads and mass spectrometry (MIB/MS) assay (23). MIB/MS and related proteomics assays have reliably provided kinome-wide determination of on- and off-target cellular activities of protein kinase inhibitors (24). Previous studies delineating ERK substrates have typically utilized a single cell line (fig. S2A). Despite the near 100% occurrence of *KRAS* mutations in PDAC, PDAC is genetically heterogeneous, with most other mutations occurring at single digit frequencies (1). Therefore, we evaluated a panel of

six $KRAS^{G12C/D}$-mutant PDAC cell lines treated acutely (1 hour) or long-term (24 hours) with SCH772984 (Fig. 2A). Using MIB/MS, we found selective inhibition of only ERK1 and ERK2 out of 207 protein kinases quantified at both time points (Fig. 2B, data S2). Thus, we confirmed the cellular selectivity of SCH772984 for ERK1/2.

To identify the ERK-dependent phosphoproteome in KRAS-mutant human cancer, we performed quantitative phosphoproteomics using phosphopeptide enrichment and LC-MS/MS in the same panel of six *KRAS*-mutant PDAC cell lines (Fig. 2C). To optimize detection of direct ERK substrates, we treated cells acutely for 1 hour. To capture both primary and secondary consequences of ERK inhibition, we performed long-term 24 hour treatment with ERKi, a time point when compensatory activities begin to appear due to loss of ERK negative feedback regulation (6). Altogether, we detected a total of 13,646 unique total phosphosites across all six cell lines. Of these, 932 were differentially regulated at 1 hour of ERKi and 4,288 were differentially regulated by 24 hours (Fig. 2D and data S3). At 1 hour, phosphosites were predominantly downregulated, whereas by 24 hours, a considerable fraction was upregulated.

A comparison of our PDAC ERK-dependent phosphoproteome with the ERK substrate Compendium showed overlap of only 12% (580) phosphosites and 33% (707) phosphoproteins (Fig. 2E). To account for phosphosites attributed to other kinases not included in the Compendium, we expanded our analysis to include the Post-Translational Modification Signatures Database (PTMsigDB) and the known regulatory sites reported by the PSP database (25), which together showed 29% (735/2,507) overlap with the ERK Compendium. Our PDAC ERK phosphoproteome showed a 21% and 60% overlap at the phosphosite and phosphoprotein level, respectively, with the combined substrates from these three datasets.

Like our analyses, the ERK Compendium data were derived from analyses of cancer-derived cell lines maintained in artificial cell culture conditions (fig. S2A). We therefore compared our ERK-dependent phosphoproteome with a recent proteomics study of pancreatic cancer patients that profiled the proteome and phosphoproteome in bulk tumor tissue including adjacent non-tumor regions, collected by the NCI Clinical Proteomic Tumor Analysis Consortium (CPTAC) (26). Our ERK-dependent phosphoproteome had a higher degree of overlap with this *in vivo* PDAC-specific dataset at both the phosphosite and protein levels: 32% and 77%, respectively (Fig. 2E). The incomplete overlap likely reflects the low cellularity of PDAC, which is typically comprised of only 10–15% tumor tissue (1). Furthermore, their analyses included only treatment-naïve PDAC, few of which were metastatic (26), whereas we evaluated cell lines derived from both primary and metastatic PDAC tumors. This suggests that our dataset is more representative of human PDAC and highlights its inclusion of more than 2,500 (>50%) phosphosites and 200 (>10%) proteins not found in any of the existing databases.

To establish how many of these phosphosites have potential regulatory functions, we compared our ERK-dependent phosphoproteome with a recent study that compiled 6,801 proteomics experiments from human cells and used machine learning techniques to assign functional significance (27). We found 91% overlap with the functional phosphoproteome

phosphosites with a median functional score of 0.43 (fig. S2, B and C). This is within a similar range of the ERK Compendium (0.47) and known regulatory sites reported in PSP (0.51) and PTMsigDB (0.54) (fig. S2C). Furthermore, when including all sites reported in PSP, only 157 sites in our ERK-dependent phosphoproteome (3%) cannot be found in any of these datasets (fig. S2B).

Two key factors contributed to the extensive depth of our dataset, such that more than 50% of our ERK regulated phosphoproteome has not been reported in previous datasets. First, we applied improved proteomics methodology enabling increased phosphosite coverage (table S1) (28–30). Second, whereas previous ERK phosphoproteomic analyses typically utilized a single cell line, our analyses of six PDAC cell lines allowed us to compensate for cell line heterogeneity.

We noted considerable heterogeneity in phosphosite coverage between cell lines, identifying from 4,000 to 10,000 total unique phosphosites, and variable numbers of ERK-regulated sites at 1 hour and 24 hours (fig. S2D). We determined that the heterogeneity of ERK-regulated sites was not related to ERK inhibitor sensitivity, but rather due to the limitation of LC-MS/MS proteomics methods to detect peptides in independent experiments. Although phosphosite detection was variable across cell lines, 75% of ERK-dependent phosphosites were detected in at least two cell lines, and we found high correlations of phosphosite changes between cell lines at each time point (fig. S2, E and F). Lastly, we performed differential expression analysis of phosphosites by considering every possible combination of one, two, three, four, and five versus all six cell lines (fig. S2G). We found that the number of unique phosphosites identified as ERK-regulated was highly dependent on how many cell lines were considered. Importantly, we found that these numbers converged on our analysis of all six cell lines that modeled cell line-specific changes. The combined dataset of six cell lines provided the highest correlation of phosphosite changes observed for any one cell line (fig. S2H). We validated a subset of 64 phosphosite and protein changes using our previously published comprehensive RPPA dataset of 13 KRAS-mutant PDAC cell lines treated for 24 hours with an equivalent concentration of SCH772984 (31). We found good agreement for those ERK-regulated phosphosites and proteins that have readily available antibodies (fig. S2, I and J). Taken together, the improved methodology applied to identify the phosphoproteome and our use of multiple cell lines contributed to the substantial extension of direct/indirect ERK substrates identified in our PDAC ERK-regulated phosphoproteome.

To determine the generality of our ERK-regulated phosphoproteome and validate our findings, we evaluated its overlap with the KRAS-dependent phosphoproteome in lung, colorectal, and pancreatic cancer cell lines. We additionally included a *Kras*-mutant mouse PDAC (KPC; $Kras^{G12D}$; $p53^{R172H}$) tumor-derived cell line to establish cross-species validation. We determined the phosphoproteome in $KRAS^{G12C}$ mutant H358 non-small cell lung cancer (NSCLC), SW837 colorectal (CRC), and MIA PaCa-2 PDAC cell lines treated with a pharmacological inhibitor of $KRAS^{G12C}$ (MRTX1257) or in the KPC mouse PDAC tumor-derived cell line treated with a RAS(ON) multi-selective tri-complex inhibitor RMC-7977 (RASi) (data S4 and S5) (32). We found that our ERK-dependent phosphoproteome was enriched in the $KRAS^{G12C}$-dependent phosphoproteomes

in human cell lines, particularly among downregulated phosphosites, where it accounted for >44% of differentially regulated phosphosites (Fig. 2F). To compare our ERK-dependent phosphoproteome in the KPC mouse cell line, we mapped the human phosphosites to the mouse reference proteome using homology alignment. Sequence alignment revealed 577 ERK-downregulated and 777 ERK-upregulated overlapping phosphosites. Among the overlapping phosphosites, 403 (70%) and 524 (67%) were significantly down or upregulated upon RASi, respectively. When considering all overlapping phosphosites between each dataset, we found high correlations (fig. S2K). These observations validate our ERK-dependent phosphoproteome as a core component of the KRAS-regulated phosphoproteome and extend our findings to the widely studied KPC mouse model.

ERK regulates a global phosphoproteome enriched in ERK interaction motifs

Extracellular stimuli promote transient ERK phosphorylation and activation, resulting in ERK translocation from the cytoplasm to the nucleus (5, 6). To assess the subcellular distribution of activated ERK under conditions of sustained activation by mutant KRAS, we applied two approaches. First, we performed immunofluorescence using an ERK1/2 phosphospecific antibody that recognizes MEK1/2 phosphorylation at the ERK1/2 TEY motif. We detected steady-state pERK and total ERK throughout the cell, including localization within the nucleus (Fig. 3, A and B, and fig S3, A and B). Following 24 hours ERKi treatment, pERK levels were strongly suppressed both outside and inside the nucleus. Concurrently, consistent with loss of ERK signaling, we observed decreased expression of the ERK substrate MYC, (fig. S3, C and D). Second, since pERK may not accurately monitor ERK activity, we used a set of ERK Kinase Activity Reporters (EKAR4) targeted to cytoplasmic (cyto-EKAR4) or nuclear (nuc-EKAR4) compartments (29). These reporters likewise showed strong suppression of both cytoplasmic and nuclear ERK activity following 24 hours of ERKi treatment (Fig. 3, C and D, and fig. S3, E and F).

We next evaluated the ERK-dependent phosphoproteome for the subcellular distribution of ERK-regulated phosphoproteins. We observed changes in phosphoproteins associated with every major organelle (Fig. 3E), consistent with ERK regulating a global phosphoproteome spanning all subcellular compartments (21). Downregulated phosphoproteins were enriched in cytoskeletal proteins at both 1 hour and 24 hours of ERK inhibition. At 24 hours, downregulated phosphoproteins were also enriched in nuclear proteins whereas upregulated phosphoproteins were enriched in plasma membrane-associated proteins.

We then determined gene set enrichment for the subcellular compartments enriched in ERK-regulated phosphoproteins. At 1 hour, downregulated cytoskeleton-associated phosphoproteins were involved in mitosis and RAS homolog (RHO) small GTPase signaling (fig. S3G). At 24 hours, additional cell cycle- and mitosis-related gene sets were associated with the cytoskeleton, with RHO GTPase signaling still enriched but no longer among the top ten significant gene sets (fig. S3H and data S6). Nuclear-associated phosphoproteins exhibiting downregulated phosphosites revealed more cell cycle-related pathways, including S phase, G2/M checkpoints, DNA replication, RNA polymerase II transcription, tRNA processing, and mRNA transport (fig. S3I). Phosphoproteins associated with the plasma membrane exhibiting upregulated phosphosites were enriched in receptor

tyrosine kinase (RTK) signaling, transport of small molecules, apoptotic proteins, and cell-cell communication (fig. S3J). Taken together, we found that ERK inhibition led to changes in phosphorylation throughout the cell, with enrichment in subcellular localizations that differed between 1 hour and 24 hours of ERK inhibition. The top pathways among ERK regulated subcellular compartments are involved in regulation of cell cycle transitions, replication, RHO GTPase signaling, and RTK activation.

ERK regulates diverse signaling pathways through direct substrate interactions that propagate to secondary, indirect interactions that promote ERK activity at the subcellular level (5, 6). One approach that can provide an approximate indication of direct ERK substrates is to characterize the phosphoproteins for the presence of the minimal ERK phosphorylation motif, [S/T]-P (33), together with two distinct ERK docking sequences, DEF (also called docking site for ERK FXF or F) and D (also called DEJL) motifs (34). These ERK docking sites enhance the specificity and affinity of ERK substrate association. We found enrichment in all three ERK-directed motifs at each time point among the downregulated phosphosites, with ~75% having the [S/T]-P motif and ~40% having a D and/or DEF motif together with [S/T]-P (Fig. 3F). Subcellular localization of ERK can direct ERK-regulated processes (35), and ERK interacting motifs have been suggested to direct ERK activity to substrates in distinct subcellular compartments (36). Therefore, we determined the subcellular enrichment of ERK-interacting motifs among ERK-regulated phosphoproteins and found distinct patterns, with D motifs enriched in each compartment while DEF motifs were primarily localized to nuclear proteins (Fig. 3G and fig. S3K). We then evaluated the identified ERK-regulated subcellular pathways for ERK-binding and phosphorylation motifs. We found a high frequency of proteins containing DEF, D, and [S/T]-P motifs. At 1 hour ERKi, ERK-binding motifs were found in 43% (16/37) of the cytoskeleton-associated phosphoproteins in the top enriched pathways, and 62% (23/37) contained a [S/T]-P ERK phosphorylation motif (Fig. 3H). This increased to 57% (24/42) and 81% (34/42) of phosphoproteins with ERK-binding motifs and [S/T]-P ERK phosphorylation motif, respectively, among cytoskeleton-associated phosphoproteins at 24 hours ERKi (fig. S3L). Among nuclear-associated phosphoproteins enriched at 24 hours ERKi, 55% (113/204) contained ERK-binding motifs and 72% (286/398) a [S/T]-P motif (fig. S3M). These results highlight that ERK can engage a multitude of phosphoprotein candidates throughout subcellular compartments to impact diverse cellular processes.

We next evaluated the importance of ERK interaction with D and DEF motif-containing proteins in supporting KRAS-dependent PDAC growth. Point mutations that selectively impair rat ERK2 interaction with D or DEF motif-containing substrates but not its kinase function have been described previously (36). We introduced the analogous amino acid substitutions into activated human ERK1^{SD} or ERK2^{SD} to generate variants impaired in interaction with D (D338N and D321N; ERK1^{SDN} and ERK2^{SDN}, respectively) or DEF (Y280A and Y263A; ERK1^{SDA} and ERK2^{SDA}, respectively) motif containing substrates. Pa16C cells stably infected with lentivirus vectors encoding each ERK1/2 mutant were then treated with Dox to transiently express each ERK mutant prior to treatment with various inhibitors (Fig. 3I, and fig. S3N). As shown previously, ERK1/2^{SD} expressing cells were resistant to G12Di or MEKi treatment while remaining sensitive to ERKi, whereas this resistance was lost in the ERK1/2$^{SDN/SDA}$ mutants (Fig. 3J, fig. S3, O, P, and Q). Ectopic

expression of ERK1/2^{SDN} or ERK1/2^{SDA} was unable to rescue ERK activation (pRSK and MYC) in cells treated with G12Di (Fig. 3I and fig. S3N). Thus, ERK interaction with D and DEF motifs is required to mediate ERK signaling critical for KRAS dependent growth.

ERK regulates a complex network of protein kinases

ERK substrates include proteins regulating gene transcription, protein phosphorylation and protein homeostasis that drive ERK dependent secondary signaling to alter the global transcriptome, proteome, and phosphoproteome. Therefore, we next evaluated our ERK-dependent phosphoproteome for phosphosite changes on these broad classes of proteins (Fig. 4A). Following 1 hour of ERK inhibition, we found decreased phosphosites on 33 epigenetic regulators, 31 transcription factors, 28 kinases, 16 E3 ligases, and 5 phosphatases. At 24 h, these numbers increased to 107, 98, 55, 44, and 13, respectively. Over half contained the ERK-interacting DEF and/or D motifs. Many of these proteins have known regulatory phosphosites, enabling us to evaluate changes in phosphorylations with reported regulatory consequences. After 1 hour of ERK inhibition, we found decreased regulatory phosphorylations on 3 epigenetic regulators, 10 transcription factors, 12 kinases, and 1 E3 ligase. Known associations with cancer pathogenesis include CBX3 S93, MYC S62, FRA1 S265, FOXO3 S294, EGFR T693, RAF1 S29/S642, p70S6KB S423, and NIPA S344. Similarly, at 24 hours of ERK inhibition, we found decreased regulatory phosphorylations on 16 epigenetic regulators, 19 transcription factors, 19 kinases, and 8 E3 ligases. These phosphoproteomic results are consistent with our comparison of the ERK-dependent transcriptome and proteome in KRAS mutant PDAC, where we identified transcriptional signatures attributable to ERK regulated transcription factors (7). Furthermore, we found that some ERK dependent proteins were regulated at the protein level but not transcriptionally, suggesting E3 ligase-dependent protein turnover (7). Together, these results support ERK-dependent regulation of a complex transcriptome, proteome and phosphoproteome.

To gain a better understanding of the dynamics of kinase regulation following ERK inhibition, we made use of the most comprehensive catalogue of kinase-motif specificities to date. Recently, we utilized a synthetic peptide library to profile the substrate sequence specificity of essentially all functional human serine/threonine kinases *in vitro* (37). Here, we applied this unbiased dataset to determine how ERK inhibition alters the frequency of down- or upregulation of each kinase motif. We assigned a relative kinase activity score to each kinase, using the frequency factor and significance to represent how frequently the kinase motif was differentially regulated (Fig. 4B, and fig. S4, A and B). Overall, we found significant dysregulation of members of the CGMC group of kinases involved in growth and cell cycle regulation that include CDK and MAPK kinases (fig. S4, C and D). After 1 hour of ERK inhibition, the most significantly downregulated kinase motifs were those of ERK1 and ERK2 (Fig. 4B and fig. S4A), consistent with the high selectivity of this ERKi. Among other significantly downregulated kinases were ERK-effector kinases, the RSKs (RSK2, RSK4 and p70S6KB), along with other MAPKs (ERK5 and p38α/β/γ), whereas, after 24 hours of ERK inhibition, we observed strong downregulation of CDKs (CDK1–6) (Fig. 4B and fig. S4B). Although ERK1/2 activity remained significantly depressed at 24 hours, it had rebounded compared to 1 hour (Fig. 4B). Interestingly, ERK1 rebound was

more significant than ERK2, perhaps reflecting differential regulation of their kinase activity despite their identical phosphorylation motif preferences (fig. S4E). Similarly, kinases downstream of ERK such as the RSKs had rebounded by 24 hours. We also observed upregulation of the related HIPK, CLK, and DYRK kinases that have not been identified previously as ERK targets. These global motif analyses revealed unexpected insights into the complexity and dynamics of kinome reprogramming that occurs after ERK inhibition.

Kinase-substrate relationships remain challenging to predict, as they are highly transient and rely on many factors such as co-localization, affinity, and kinase regulation. We utilized our recently established *in vitro* kinase-motif specificities and kinase activities dataset (37), together with the kinase-phosphosite specificities catalogued by the PSP kinase substrate database, the kinase-substrate binding interactions in PhosphoNetworks (38), and interactors catalogued by BioGRID (39). Accounting for the activities of phosphatases in our analysis is also challenging because their motif specificities and substrates are less-well defined. Nevertheless, we performed enrichment analyses of potential phosphatase-substrate relationships from BioGRID, and found dysregulation of only a few phosphatases, namely the ERK-selective dual specificity phosphatases (DUSP2, DUSP3, DUSP6), cell cycle control phosphatases (CDC14B and CDC25A), and AGC kinase phosphatases (PHLPP1/2) (fig. S4, F and G). Therefore, we focused on kinase-substrate specificities and changes we observed in our phosphoproteomics data to develop a network analysis method (fig. S4H).

This network assigns interaction scores for every phosphosite in our dataset using supporting data from kinase-phosphosite and kinase-phosphoprotein interactions (fig. S4I). Importantly, this method incorporates previously reported kinase-substrate relationships, which is heavily biased towards the most-studied kinases, by strengthening kinase-substrate interactions we derived by motif analysis (data S7). Kinase-substrate interactions that have not been previously reported but are supported by motif specificities remain a main component of the network, and this is reflected in their interaction score. For example, top scoring interactions were mainly attributed to *MAPK3*/ERK1, driven mostly by motif specificity score and further increased by interactions reported in previous datasets (fig. S4I). Despite their identical phosphorylation motif preferences, ERK1 displayed slightly higher activity than ERK2 in our *in vitro* kinase assay (fig. S4E), which biased interactions more towards ERK1 than ERK2 in our analyses.

Using this kinase-substrate network, we evaluated the top-scoring interactions and differential kinase activities following 1 hour and 24 hours of ERK inhibition (Fig. 4C and fig. S4J). Following 1 hour ERK inhibition, the downregulated kinase networks were mainly attributed to ERK1/2, RSK2/4, and p70S6KB. Motif analysis of phosphosites attributed to ERK from this network revealed an enrichment of the prototypical [P/L/V/I]-X-p[S/T]-P motif (fig. S4K). Additionally, when we considered positional depletion, we noted strong negative selection of basic residues (K/R) at the −3 position, and acidic residues (D/E) at positions +1 to +3. This further defines the stringency of ERK1/2 phosphomotifs. We then analyzed RSK2/4 phosphosites and found enrichment of basic residues at positions N-terminal to the phosphorylation site, consistent with previous studies (40), and depletion of proline at +1 (fig. S4K), exhibiting mutual exclusive substrate preferences as ERK

and targeting a distinct subset of phosphorylation sites. These motifs have been well characterized (25, 37), validating our network construction.

The cyclin-dependent kinases CDK1–6 make up the predominant downregulated phosphorylation network after prolonged ERK inhibition (Fig. 4C). While CDK substrates overlapped with a subset of ERK substrates, ERK1/2 also maintained a distinct group of substrates. CDKs are also CMGC family proline-directed kinases, and therefore distinguishing CDK from ERK MAPK phosphosites relies on subtle motif differences. When we investigated CDK1–6 phosphorylations from our network we found the motif to be enriched for proline at +1, as expected, and basic residues (K/R) at the +3 position (fig. S4K). This is consistent with the motif specificity that we reported where there was a near complete requirement of K/R at +3 for CDK activity (37). We also observed a depletion of basic residues N-terminal to the phosphorylation site and acidic residues in the C-terminal region, further adding specificity to these kinase motifs. With ERK1/2 and CDK1–6 having similar but distinct motif specificities, these results highlight the high probability that ERK and CDK target sequences overlap (e.g., [P/L/V/I]-X-[S/T]-P-X-[K/R]). When we evaluated our ERK regulated sites for this sequence we found 266 phosphosites, half of which contained D or DEF motifs (132/266). Furthermore, these sites are found on mediators of PDAC growth, for example, MYC at S62 (P-L-S*-P-S-R), that are likely to be under convergent regulation by MAPKs and CDKs.

Unexpectedly, after sustained ERK inhibition, we observed upregulation of a group of kinases not known to be ERK substrates, including HIPK (HIPK1–3), DYRK (DYRK3, DYRK1A/B), and CLK (CLK1/4) kinases (Fig. 4, B and C, and fig. S4, B and D). We speculate that these comprise compensatory mechanisms to offset the deleterious cellular consequences of ERK inhibition. Consistent with this possibility, our DepMap analyses found that several (HIPK1, DYRK1A/B, and CLK1/4) showed genetic dependencies in PDAC comparable to ERK1 (*MAPK3*) and ERK2 (*MAPK1*) (fig. S4L). These proline-directed kinases make up a distinct branch of CMGC kinases (fig. S4D). The phosphorylation motif enrichment pattern for DYRK family kinases favored proline residues in the +1 and +3 positions with a basic residues N-terminal to the phosphorylation site (fig. S4K). This p[S/T]-P-X-P motif has been previously attributed to ERK1/2 (21). However, our motif and network analyses revealed that, although the DYRK/HIPK/CLK kinases are proline-directed, they are likely targeting a distinct subset of S/T-P substrates from those of ERK1/2 or CDK1–6 and are regulated in the opposite direction in response to ERK inhibition. These results further suggest that they represent a group of substrates resulting from compensatory activities due to prolonged ERK inhibition.

We then investigated the mechanisms of the robust downregulation of CDK activity by sustained ERK1/2 inhibition. CDKs are regulated at the level of transcription, post-translational modification, and through protein-protein interactions with their cyclin activators (41). We found that all CDKs were downregulated by 24 h, both transcriptionally and at the protein level, along with many of their associated regulatory cyclins (fig. S4M). However, we noted that cyclin B1 and B2 were the most significantly downregulated proteins even though their transcript levels were unchanged, suggesting that their protein levels are regulated through degradation. We found decreased phosphosites on members of

the anaphase promoting complex/cyclosome (APC/C) proteins known to regulate cyclin B1 and B2. After 1 hour ERK inhibition, we observed downregulation of ANAPC1 S688 and *CDC27*/ANAPC3 S344, attributed to ERK1/2 (fig. S4N). By 24 hours of ERK inhibition, we found several downregulated phosphosites on CDC20 (S41, T59, T106, and T170) and FZR1 (T121), both of which are known regulatory components of the APC/C (fig. S4M). Taken together, we found that ERK inhibition leads to a coordinated collapse of CDK activity regulated at the levels of gene transcription, protein phosphorylation, and protein degradation. This collapse of essentially every key cell cycle regulatory CDK contributes to the potent cell cycle arrest, rather than apoptosis, caused by ERK inhibition in KRAS-mutant PDAC cells (42, 43).

We then evaluated the dysregulated kinases in our KRAS-regulated phosphoproteomes. Although KRAS can engage multiple effectors to regulate a diverse network of signaling cascades, we found few differences between ERK- and KRAS-regulated kinases (Fig. 4D). Notably, the PI3K effector AKT was downregulated in only one of four cell lines (H358). The most consistently downregulated kinases across the KRAS-regulated kinomes were the cyclin-dependent CDKs, ERK MAPKs, and RSKs. Upregulated kinases showed more cell line heterogeneity, with HIPK and DYRK kinases the most consistent, validating our findings from the ERK-dependent kinome. Few KRAS-regulated kinases were significantly dysregulated in the opposite direction to ERK. This is consistent with our observation that ERK activity is sufficient to rescue KRAS inhibition and is enriched in the KRAS-regulated phosphoproteome.

ERK is highly integrated with RHO signaling

To gain mechanistic insight into the cellular processes regulated by the PDAC ERK phosphoproteome compared with the ERK Compendium, we performed pathway analysis using all gene sets in the Gene Ontology (GO), KEGG and Reactome databases. We compared the overlap of both significantly enriched gene sets and all terms, significant or not, associated with each ERK-regulated phosphoprotein list (Fig. 5A and fig. S5A). Despite only 33% phosphoprotein identity (Fig. 2E), we found 66% overlap of the PDAC ERK-dependent phosphoproteome with the ERK Compendium (Fig. 5A and fig. S5A). Although the non-overlapping enriched gene sets exceeded the number of overlapping sets (674 non-overlapping versus 563 overlapping) using the above criteria, the overlap was greater (85%) when we considered any associated GO, KEGG, or Reactome terms.

Our dataset was most enriched in genes encoding proteins related to RHO GTPase signaling pathways (Fig. 5B), which were also among the top gene sets enriched in the ERK Compendium. The top pathways significantly enriched in our PDAC ERK-dependent phosphoproteome that were not significant in the ERK Compendium were related to chromatin organization, RNA processing, and G1/S cell cycle components (Fig. 5B). Thus, our identified ERK-dependent phosphoproteome revealed a more comprehensive profile of the role of aberrant ERK activation in supporting KRAS-dependent cellular properties of PDAC.

We also found that the shorter 1 hour ERK inhibition altered kinases and substrates distinct from those altered upon longer 24 hour ERK inhibition. Therefore, we evaluated gene set

enrichment using Reactome gene sets in down- and upregulated phosphoproteins at both time points. After 1 hour ERK inhibition, we found enrichment of RHO GTPase- and EGFR- or MAPK-associated signaling pathways in the downregulated phosphoproteins (Fig. 5C and data S8). No gene sets were enriched among the upregulated phosphosites. By 24 hours of ERK inhibition, we found a different set of significantly enriched pathways among down- and upregulated phosphoproteins. Downregulated phosphoproteins were enriched in components of the cell cycle, mitosis, chromosome maintenance, DNA damage and replication. Notably, contrary to the enrichment of RHO GTPase phosphoproteins with downregulated phosphorylations after 1 hour ERK inhibition, at 24 hours these same RHO-regulated pathways were enriched among the upregulated phosphoproteins. The distinct nature of processes altered upon longer-term ERK inhibition likely reflects secondary activities initiated by the acute loss of ERK function, particularly compensatory activities in response to the growth suppression induced by ERK inhibition.

We then focused on RHO GTPase-associated genes to examine their switch from enrichment in downregulated phosphoproteins after 1 hour ERK inhibition to enrichment in upregulated phosphoproteins after 24 hour ERK inhibition. We analyzed the phosphosites on proteins within the RHO GTPase Reactome pathway and how these changed over time (fig. S5B). Very few phosphosites downregulated at 1 hour were upregulated after 24 hours. Instead, upregulated and downregulated phosphosites were distinct at each time point. We then used our phosphorylation network consisting of both time points to isolate the proteins and respective kinases within these gene sets (Fig. 5D). This analysis revealed three distinct regulatory networks. The first consists of ERK substrates with downregulated phosphosites after 1 hour ERK inhibition. The second consists of CDK1/2/3/5/6 substrates downregulated after 24 hours ERK inhibition, which shared a subset of substrates with ERK1/2. The third is comprised of upregulated phosphosites on a distinct group of protein substrates driven by putative compensatory activation of PKN1/2, PAK4/6, PDPK1, and DYRK/HIPK/CLK/SRPK kinases.

The RHO GTPase-associated kinases PKN1/2, PAK4/6, and PDPK1 have well-described associations with regulation of RHO-dependent F-actin cytoskeletal reorganization, indicating that our network analysis identified mechanistically relevant associations. The network interactions responsible for identifying PKN1/2, PAK4/6, and PDPK1 were comprised of distinct phosphorylation motifs (fig. S5C) that were found on actin cytoskeleton-associated proteins, such as EXOC2, PXN, AHNAK, or SHROOM3 (fig. S5D).

RHO GTPase signaling is dynamic and complex; consequently, RHO signaling pathway genes overlap with numerous other cellular functions. To further characterize ERK-dependent changes in the RHO GTPase network, we identified proteins that had either downregulated or upregulated phosphorylations upon ERKi treatment at either timepoint, then performed gene enrichment analyses. Among the proteins with downregulated phosphorylations, we found that RHO GTPase signaling overlapped considerably with gene sets encoding proteins related to RTK signaling and cell cycle regulation (fig. S5E). However, upregulated phosphorylations were associated primarily with more restricted RHO GTPase gene sets, such as RAC1, RAC3, CDC42, and RHOA. The only RHO GTPase-

associated proteins that contained both downregulated and upregulated phosphorylations were PXN, *PPP1R12A*/MYPT1, *CTTN*/EMS1, *ARHGEF18*/P114RhoGEF, *ARHGAP29*/PARG1, and *SCRIB*/SCRB1. We considered that these phosphorylation changes could be secondary to changes in total protein levels. However, few proteins were altered in their expression levels and no consistent trends were observed (fig. S5F). Overall, the upregulated phosphorylations were largely associated with regulation of RHO GTPase activity. In contrast, the downregulated phosphorylations are largely associated with functional pathways such as cellular growth control and morphology that are in turn regulated by the confluence of signaling from RTKs, MAPKs and RHO GTPases.

A well-studied consequence of RHO activation is promotion of actin cytoskeleton reorganization that drives alterations in cellular morphology (44). We used immunofluorescence microscopy to evaluate changes in actin stress fibers following 24 and 72 hours of ERK inhibition. Consistent with our phosphoproteomics analyses, an increase in actin stress fibers was observed within 24 hours of ERK inhibition and continued at and beyond 72 hours (Fig. 5, E and F). These results were also consistent with our observations of cellular flattening and increased cell size (fig. S5, G and H) during growth assays following ERK inhibition. RHO promotion of actin stress fibers can activate YAP1 (44), a well-validated driver of KRAS independence (45, 46). Consistent with RHO activation acting as a compensatory mechanism, RHOA and YAP1-TEAD activation was identified as a basis for acquired resistance to adagrasib in $KRAS^{G12C}$-mutant cancer cell lines (47, 48).

ERK regulates proteins critical for PDAC growth

While specific ERK substrates have been evaluated for their involvement in driving the growth of KRAS-mutant PDAC (e.g., MYC) (49), a systemwide determination of the full spectrum of ERK-regulated proteins that drive cancer cell growth remained to be done. To begin to elucidate the cancer driver components of the ERK-dependent phosphoproteome in PDAC, we first evaluated the genetic dependency of all ERK regulated phosphoproteins, using the genome-wide CRISPR/Cas9 data on 43 KRAS-mutant PDAC cell lines in the DepMap database. Of the 1,636 genetic dependencies (median Chronos <-0.5) identified in *KRAS*-mutant PDAC cell lines, we detected 690 in our phosphoproteomics dataset, over half (362) of which had ERK regulated phosphosites (fig. S6A).

We and others have established that ERK-regulated proteins can be found throughout the cell. An unresolved question is whether ERK nuclear or cytoplasmic activity is more critical for cancer cell growth (50–52). We annotated the top localization scores for each protein with strong genetic dependencies in PDAC and found enrichment in nuclear-associated phosphoproteins (76%; 288/1,072) (Fig. 6A). We also found an appreciable number (36%; 136/406) of cytoplasmic proteins, consistent with ERK regulating critical proteins in both the nucleus and cytoplasm.

Having found RHO GTPase-related gene sets enriched among the ERK-regulated phosphoproteins, we next evaluated the genetic dependencies of RHO GTPase phosphoproteins. Indeed, among the high genetic dependencies we found significant enrichment in RHO GTPase effectors and the more focused RHOBTB GTPase pathway. Gene set enrichment of all high dependency ERK-regulated phosphoproteins revealed RNA

metabolism and cell cycle components as top enriched pathways, particularly cell cycle pathways relating to M phase and S phase (Fig. 6A and fig. S6B). This is consistent with ERK regulating nearly every principal component of the cell cycle machinery.

We next considered whether ERK-regulated genetic dependencies were selective for *KRAS*-mutant cancers. As over 90% of PDAC cases harbor mutant KRAS, leaving few WT KRAS PDAC cell lines to compare, we extended our analysis to include other *KRAS*-mutant cancers with at least 10% representation of KRAS mutation frequency in DepMap (fig. S6C). We defined *KRAS*-mutant as harboring specific known KRAS driver mutations including G12A/C/D/R/S/V, G13D, or Q61K/H/L/R. We compared the genetic dependencies in cell lines harboring mutant KRAS to those in lines harboring WT KRAS. Of the genes with significantly greater dependencies in KRAS mutant versus KRAS WT cancers, we found 23 genes whose protein products include ERK-regulated phosphosites (Fig. 6B). These mutant KRAS-selective genetic dependencies were even more apparent in KRAS mutant PDAC versus all KRAS mutant cancers (Fig. 6C). This result suggests that these proteins, while important for supporting proliferation across cancer types, may be even more crucial in PDAC, perhaps due to its higher dependence on KRAS and sustained ERK activity.

Among the top mutant KRAS-selective ERK targets were *FOSL1*/FRA1, MYC, and *BCAR1*/p130CAS. We and others recently established essential roles for FRA1, MYC, and p130CAS in supporting KRAS mutant PDAC tumorigenic growth (43, 49, 53). Other genes/proteins with selective dependencies in KRAS mutant cancer types are involved in actin cytoskeleton organization and RHO GTPase regulation (FLII, *ARHGEF7*/COOL1, NRBP1), epigenetic modifiers (*WDR77*/MEP50, RIOK1), metabolic proteins and small molecule transporters (SCAP, SCD, IMPDH2, ENO1, TPI1, NME2, EFR3A, LSM12, ABCF1, WNK1, TRPM7), or DNA replication and RNA metabolism (DBF4, POLR1A, NIFK, NPM1).

Having evaluated the genetic dependencies of the entire ERK-regulated phosphoproteome, we next leveraged our kinase-substrate network to attribute kinase interactions associated with high dependency genes (Fig. 6D). This revealed genetic dependencies that were identified as ERK1/2 substrates, substrates of the downstream ERK1/2 kinases RSK1/3/4, and CDK substrates. We found that most genetic dependencies were associated with downregulated phosphosites, not upregulated phosphosites. The highest genetic dependencies attributed to ERK1/2 phosphorylation at 1 hour ERKi were MYC, *CDC27*/ANAPC3, ANKLE2, and ANAPC1. Notably, ANKLE2, ANAPC1 and ANAPC3 are mitotic regulators, and ANAPC1/3 are core components of the APC/C that regulate the CDK1 activators cyclin B1 and B2 (fig. S4, M and N). We determined that concurrent pharmacologic inhibition of APC/C and ERK synergistically suppressed PDAC growth (7).

Among the top genetic dependencies in the ERK-regulated PDAC phosphoproteome were the CDK1 regulators PKMYT1 and WEE1, and CDK1 itself. These observations lead to a model whereby ERK regulates phosphoproteins that drive CDK1 activation and progression through S and M phases of the cell cycle. This activity would likely cooperate with the second most frequent genetic driver in PDAC, mutational loss of the CDK4/6-regulating

tumor suppressor *CDK2NA*, which occurs at almost as high a mutational frequency (90%) as *KRAS* and is required for PDAC progression in mouse models (1, 54).

Discussion

In summary, our delineation of the ERK-dependent phosphoproteome specifically in the setting of persistent hyperactivation in KRAS-mutant cancers has substantially expanded both the depth and breadth of ERK-regulated phosphoproteins. Together with our complementary determination of the ERK-dependent transcriptome in KRAS-mutant cancers (7), we have established to date the most comprehensive molecular portrait of the consequences of pathologic ERK signaling, which controls a multitude of cellular processes that disrupt normal cell cycle regulation. Despite the plethora of KRAS effectors now identified, our studies nevertheless establish the dominant role of the RAF-MEK-ERK signaling network in driving KRAS-mediated oncogenesis. Our analyses also reveal the highly dynamic response of the kinome to KRAS-ERK inhibition, with the delayed onset of adaptive secondary / compensatory activities that may drive both primary and treatment-associated acquired resistance mechanisms to KRAS and ERK inhibition.

Specifically, we present ERK signaling as highly integrated with RHO GTPase and CDK signaling, and report pathway components that will be of interest for further study to determine their functional role in supporting KRAS mutant PDAC and other KRAS mutant cancers. The recent approval of direct KRAS inhibitors marks a major milestone in treatment of KRAS mutant cancers. However, the rapid onset of acquired resistance driven largely through ERK reactivation also emphasizes that full elucidation of how ERK supports KRAS oncogenic function will be critical for the clinical advancement of KRAS inhibitors that are effective for long-term treatment of these cancers.

Materials and Methods

Cell culture

Patient-derived xenograft (PDX) human PDAC cell lines (Pa01C, Pa02C, Pa03C, Pa14C, and Pa16C) were provided by Dr. Anirban Maitra (MD Anderson Cancer Center). Murine KPC tumor-derived cell line (K8484) was provided by Dr. Ken Olive (Columbia University). PDAC cell lines (AsPC-1, HPAC, MIA PaCa-2, PANC-1, and SW1990), NSCLC cell line (H358), CRC cell line (SW837), and HEK293T were obtained from American Type Culture Collection (ATCC). PDX-derived, KPC, and CRC cell lines were maintained in Dulbecco's Modified Eagle medium (DMEM) supplemented with 10% fetal bovine serum (FBS). Conventional PDAC and NSCLC cell lines were maintained in RPMI 1640 medium supplemented with 10% FBS. The identity of PDAC lines were verified by short tandem repeat analysis. All cells were tested and negative for mycoplasma.

Expression plasmid constructs

ERK1 and ERK2 wild-type human cDNA was myc-tagged and cloned into a pCEFL construct. Site-directed mutagenesis using the primers listed in Table S1 were used to generate single, double, and triple ERK1 and ERK2 mutants. Following sequencing verification, AGE1-myc-tagged FWD and ERK1/2-MLU1 REV primers (table S2) were

used to amplify ERK1 and ERK2 cDNA containing the desired point mutation(s). The purified PCR inserts and pINDUCER-EGFP (55) were digested with AGE1 and MLU1, purified, and ligated together. Colonies were screened via sequencing upstream, downstream, and within the insertion sites to cover the entire inserted region. Resultant plasmids containing Myc-tagged ERK1 and ERK2 constructs in the pINDUCER backbone were deposited to Addgene (Plasmid numbers: 213591 (R84S), 213592 (S170D), 213593 (R84S/S170D, 213594 (R84S/D338A), 213595 (R84S/S170D/D338N), 213596 (R84S/S170D/Y280A), 213597 (R67S/S153D), 213598 (R67S/S153D/D321N), and 213599 (R67S/S153D/Y263A). EKAR4 constructs with or without nuclear localization sequence (nuc-EKAR4) or nuclear export sequence (cyto-EKAR4) were gifts from Dr. Jin Zhang (UCSD) and were described previously (35, 56). Using the EKAR-BAMH1 FWD and UT/NLS/SAL1 REV primers, the EKAR constructs were amplified and cloned into pLenti CMV GFP Hygro (656–4) (Addgene Plasmid #17446). Both the purified PCR inserts and pLenti GFP Hygro were digested with BAMH1 and SAL1, purified, and ligated. Colonies were screened as described above.

Inhibitors

The ERK1/2-selective inhibitor SCH772984 was provided by Merck. The MEK1/2-selective inhibitor, trametinib (GSK1120212), was obtained from Selleckchem, cat. no. S2673. The $KRAS^{G12C}$-selective inhibitor MRTX1257 was provided by Mirati Therapeutics. The $KRAS^{G12D}$-selective inhibitor MRTX1133 was provided by Mirati Therapeutics or purchased from Selleckchem, cat. no. E1051. The RAS(ON) multi-selective tri-complex inhibitor RMC-7977 was provided by Revolution Medicines.

Antibodies

The following primary antibodies were used for immunoblotting and/or immunofluorescence staining. From Cell Signaling Technology: p44/42 MAPK (ERK1/2) (L34F12), cat. no. 4696 (RRID:AB_390780); phospho-p44/42 MAPK (ERK1/2) (Thr202/Tyr204) (D13.14.4E), cat. no. 4370 (RRID:AB_2315112); Myc-Tag (9B11), cat. no. 2276 (RRID:AB_331783); c-MYC (D84C12), cat. no. 5605 (RRID:AB_1903938); phospho-p90RSK (Thr359/Ser363), cat. no. 9344 (RRID:AB_331650); RSK1/2/3 (32D7), cat. no. 9355 (RRID:AB_659900); phospho-FRA1 (Ser265) (D22B1), cat. no. 5841 (RRID:AB_10835210). From Sigma-Aldrich: Vinculin, cat. no. V9131 (RRID:AB_477629); KRAS (3B10–2F2), cat. no. WH0003845M1 (RRID:AB_1842235). F-actin was stained using phalloidin Alexa Fluor™ 488, Invitrogen cat. No. A12379, and Alexa Fluor™ 647, Invitrogen cat. No. A22287. Secondary antibodies used for immunoblotting included IgG (H+L) cross-adsorbed goat anti-mouse, HRP, Invitrogen cat. no. PI31432, and IgG (H+L) cross-adsorbed goat anti-rabbit, HRP, Invitrogen cat. no. PI31462. Secondary antibodies used for immunofluorescence included goat anti-mouse IgG (H+L) Alexa Fluor™ 568, Invitrogen cat. no. A-11004, goat anti-rabbit IgG (H+L) Alexa Fluor™ 568, Invitrogen cat. no. A-1101, and goat anti-rabbit IgG (H+L) Alexa Fluor™ 488, Invitrogen cat. no. A-11008. Antibodies used for RPPA are listed in table S3.

Viral transduction

HEK293T cells (0.9×10^6) were plated in T25 flasks in DMEM supplemented with 10% FBS. After 24 hours the cells were transfected using 500 µl of Optimem combined with 25 µl of Fugene 6 (Promega), 3 µg of psPax, 1 µg of pMD2.G, and 4 µg of target construct. After 24 hours the medium was replaced with DMEM supplemented with 20% FBS. Viral particles were generated over 48 hours at which point supernatant was removed and filtered through a 0.45 µm PES syringe filter (Nalgene). Filtered supernatant was either aliquotted and frozen at −80°C or used directly to infect target cells. Supernatant was combined with polybrene (8 µg/ml) and diluted in either DMEM or RPMI with 10% FBS to infect. Culture medium was changed 12 hours post infection and selection was initiated 48 hours after transduction.

siRNA transfections

All siRNA transfections were performed using lipofectamine RNAiMax (ThermoFisher, cat. no. 13778150), and 10 nM of siRNA in Optimem. RNAiMax was added to Optimem and incubated for 5 min at room temperature, then siRNA(s) were then added and incubated 20 min. The siRNAs and cells were combined and incubated for 72 hours for cell lysates or 6 days for growth assays. Non-targeting controls were used in each experiment. The siRNAs utilized are listed in table S4.

Growth assays

Cells were plated in 96-well plates (1,000–2,000 cells per well) and grown for 24 hours. An additional day 0 plate was also prepared. For Dox inducible cell lines, either Dox or vehicle (DMSO) was added to cells during plating. Pharmacological inhibitors were added to cells after 24 hours using a Tecan D300e digital dispenser; additionally, the day 0 plate was labeled with calcein AM (cells) or Hoechst (nuclei) and counted live. Treated cells were incubated for designated times. Calcein AM or Hoechst was added and were counted using either a SpectraMax i3X multimode detection platform (Molecular Devices) for calcein AM labeled cells and a BioTek Cytation 1 (Agilent) for Hoechst labeled cells. Day 0 plates were used to calculate fold growth to verify cells were growing as expected between biological replicates. Growth percentage was calculated for each biological by normalizing treated values to their control samples, which were set to 100%. Three-parameter drug response curves were generated using the average relative growth (%) from ≥3 biological replicates in GraphPad Prism version 9.3.1. Error bars represent the standard error of the mean between biological replicates.

Immunofluorescence staining and imaging

Cells were plated on glass bottom dishes and imaged using an EVOS M7000 wide-field microscope with a 40X, 0.65 NA objective. Cells were fixed with 4% formaldehyde for 20 min, permeabilized with 0.1% Triton for 5 min, rinsed with PBS, and blocked using 3% BSA-PBS for 1 h, all at room temperature. Primary antibodies targeting: pERK1/2, ERK1/2, and MYC were diluted 1:200 in 3% BSA-PBS and either incubated for 2 hours at room temperature or overnight at 4°C. Cells were washed with PBS and then incubated for 45 min with Alexa-488 and/or Alexa-561 secondary antibodies diluted 1:200 in 1% BSA-PBS

at room temperature. Cells were stained for F-actin using phalloidin tagged with either Alexa Fluor™ 488 or 647. Phalloidin was diluted 1:100 in PBS and cells were stained for 20 minutes at room temperature. Nuclei were visualized by staining cells for DAPI diluted 1:10,000 in PBS for 5–10 min following secondary antibody staining at room temperature. Cells were washed multiple times using PBS and stored in PBS at 4°C until imaging.

EKAR live cell imaging

Pa16C cells stably expressing EKAR4, nuc-EKAR4, or cyto-EKAR4 were plated on glass bottom dishes and imaged live using an EVOS M7000 wide-field microscope with a 40X, 0.65 NA objective. Upon drugging, cells were washed with PBS and phenol red-free DMEM+10% FBS was added.

Image Analysis

For all images, background was removed using a sliding paraboloid in FIJI. The resulting images were analyzed using Cell Profiler. For the immunofluorescence images, the DAPI images were used to identify the primary objects (nuclei) and the total ERK1/2 antibody was used to identify secondary objects (cells). All cells and nuclei touching the edges were discarded. The integrated density for phospho-ERK1/2 was calculated within nuclei and cells, and MYC was calculated within the nuclei, where it was almost entirely localized. To quantify F-actin, primary objects (nuclei) were identified again using the DAPI images and secondary objects (cells) using the F-actin images. The integrated density for F-actin was calculated for each cell. Cell size was calculated by outlining individual cells in FIJI. For EKAR expressing cells the primary objects were identified using the YFP channel, cells touching the edge were removed, and the integrated density for each cell was measured in the CFP and FRET channels. The FRET ratio was determined by dividing the FRET value by the CFP value for each cell. For each biological replicate, the mean value of the DMSO sample was calculated and all values were divided by that mean value. From each biological replicate, 5–10 frames were collected. Since no statistical difference was observed in the relative integrated density between replicates, all nuclei/cells were grouped together. Table S5 lists the number of cells analyzed for each condition. GraphPad Prism version 9.3.1 was used for statistical analyses and removal of outliers (using Q=0.1, ROUT) (82). Significance was evaluated using a one-way ANOVA and Kruskal-Wallis test relative to DMSO.

Immunoblot analyses

Following the designated treatments, cell lysates were prepared as follows: cells were washed with cold PBS and then scraped into lysis buffer (50 mM Tris-HCl pH 7.5, 150 mM NaCl, 1% NP-40 (Igepal CA-630), 0.5% sodium deoxycholate, 0.1% SDS) supplemented with protease (Roche) and phosphatase (Sigma-Aldrich) inhibitors. Lysates were incubated 10 min on ice, centrifuged at 8,000 rpm (4°C for 10 min), and supernatant was transferred to a new tube. Bio-Rad Protein Assay Dye Reagent cat. No. 5000006 was used to determine protein concentration. Equal amounts of protein were combined with 4X Laemmli SDS sample buffer and 2.5% 2-mercaptoethanol and loaded into SDS-PAGE gels. Immunoblots were performed using standard procedures. Immunoblot levels were analyzed using FIJI.

Reverse Phase Protein Array

Reverse Phase Protein Array (RPPA) was performed as previously described (31, 42, 57–61). In brief, PDAC cell lines were reverse transfected with a non-targeting (NS) siRNA or siRNAs targeting KRAS (*KRAS*), ERK2 (*MAPK1*), ERK1 (*MAPK3*), or ERK2/ERK1 (*MAPK1/3*). Two siRNAs for each gene were used and four biological replicates for each treatment were performed. A list of siRNAs used is found in Table 3. Cells were collected 72 hours post transfection and cell lysates were prepared as previously described (31, 42, 57–61). Samples were directly lysed from the 6-well plates using a buffer containing a 1:1 solution of Tissue Protein Extraction Reagent (Pierce) and 2X Tris-Glycine SDS Sample Buffer (Invitrogen Life Technologies) supplemented with 2.5% of 2 β-mercaptoethanol (Sigma Aldrich). The lysates were heated at 100°C for 8 mins and stored at −80°C until RPPA was performed.

Each sample was printed in triplicate on nitrocellulose-coated glass slides (Grace Bio-Labs) using an Aushon 2470 arrayer (Quanterix) outfitted with 185 μm pins. To ensure RPPA assay quality and data reliability, two twelve-point standard curves were prepared as previously described (62) and printed on each slide along with the samples. Before immunostaining, each slide was treated for 15 minutes at room temperature with Reblot Plus Mild Antibody Stripping Solution (MilliporeSigma) followed by incubation for five hours with I-Block (Invitrogen), a protein-based blocking reagent. Immunolabeling was performed using an automated Autostainer (Agilent Technologies). Arrays were first treated with a 3% hydrogen peroxide, biotin blocking system, and then a serum free protein block. Arrays were probed with a total of 150 antibodies (Table S2) to measure protein expression and activation of markers involved in signaling pathways that control cell growth, survival and metabolism.

Before their use on RPPA, all antibodies were rigorously validated for specificity, selectivity and optimal concentration as previously described (63). Incubation with the primary antibodies was performed for 30 minutes at room temperature followed by incubation for 15 minutes in goat anti-rabbit, mouse, or rat (Vector Laboratories) biotinylated secondary antibody. For each staining batch, one slide was incubated with the secondary antibody alone as a negative control for the nonspecific background. The commercially available GenPoint kit (Agilent Technologies) based on tyramine avidin/biotin signal amplification coupled with the fluorescent IRDye 680 Streptavidin (Li-Cor Biosciences) was used for signal detection. The total protein amount for each sample was assessed by staining one in every 15 slides with Sypro Ruby Protein Blot Stain (Invitrogen) following manufacturer's instructions. Slides were treated with a fixative solution (10% v/v methanol and 7% v/v acetic acid) at room temperature for 15 minutes, washed in deionized water, and stained with Sypro Stain for 30 minutes at room temperature in the dark. Slides were washed twice in deionized water and dried before scanning. Image acquisition for Sypro Ruby, control and antibody-stained slides was performed using a Tecan scanner (TECAN) using two different wavelength channels at 580 nm (for the Sypro stained slides) and 620 nm (for the antibody stained and control slides). Data analysis was performed using MicroVigene software, version 5.1.1.1 (VigeneTech, Inc). This software includes automatic spot finding, background subtraction, total protein normalization and replicates average as previously

described (64). The final RPPA intensity value output for each sample is the average of the replicates printed on the arrays, a single value for every marker analyzed in this study.

Antibody intensities were $\log_2$ transformed and median centered by the NS control. Differential expression was performed by linear models for microarray and RNAseq data (LIMMA) (65, 66). When considering all cell lines together, individual cell lines were used as a blocking term (67).

RNA-seq analysis

RNA-sequencing was conducted on Pa16C cells expressing $ERK1^{SD}$, $ERK2^{SD}$, or GFP upon 24 hours treatment with KRASi (MRTX1133) or control (DMSO). Total RNA was isolated from Pa16C cells constitutively expressing activated $ERK1^{SD}$ (R84S/S170D), $ERK2^{SD}$ (R67S/S153D), or GFP control treated for 24 hours with 100 nM MRTX1133 or equivalent DMSO. Two biological replicates were prepared for each condition. cDNA libraries were prepared from mRNA isolated by poly(A) mRNA strand purification of total RNA by Novogene (Sacramento, CA) and sequenced on an Illumina NovaSeq2000. RNA-seq data analyses were performed as described (7). Repressed gene expression was determined by comparing expression changes of top differentially expressed genes ($|logFC| > 0.25$, $FDR < 0.01$) in GFP control cells to $ERK1^{SD}$ or $ERK2^{SD}$ expressing cells. ERKi treatment followed by RNA-seq of PDAC cell lines (HPAC, HPAFII, Pa01C, Pa04C, Pa14C and PANC-1) was described previously (31).

RNA-seq data preprocessing and analyses

TrimGalore (v0.4.5) (68) was used for QC and to trim adapters of RNA-seq data where necessary, retaining paired end reads of greater than 35 bases in length and over 28 quality score (Sanger/Illumina 1.9). The human genome version hg38 (GRCh38.p12) was used for alignment with STAR (v2.7.8a) (69) and the Gencode (v30) (70) basic transcriptome. Transcripts were quantified using Salmon (v0.11.3) (71) and then summarized at the gene level with tximport (v1.22.0) (72). BiomaRt (v2.50.3) (73) was used for annotation and edgeR (v3.36.0) was used for data management (74). Autosomal and X-linked protein coding genes were evaluated with TMM (75) normalization and differential expression comparisons with the glmQLFTest function (edgeR).

Kinome enrichment – MIB/MS

Data for cell lines treated for 24 hours with SCH772984 (1 μM) and subjected to MIB/MS analyses were published previously (76) (PRIDE ID: PXD025819). Data for cell lines treated for 1 hour with SCH772984 (1 μM) were generated as described previously (76). Briefly, lysates from treated cells were prepared in MIB/MS lysis buffer (50 mM HEPES [pH 7.5], 0.5% Triton X-100, 150 mM NaCl, 1 mM EDTA, 1 mM EGTA, 10 mM sodium fluoride, 2.5 mM sodium orthovanadate, protease inhibitor cocktail (Roche), 1% each of phosphatase inhibitor cocktails i and ii (Sigma-Aldrich). Lysates were sonicated 4x with 15-second pulses followed by centrifugation (10 minutes, 13,200 rpm, 4°C). Supernatants were clarified by 0.2 mm filter and stored at −80°C. Lysates were passed over multiplexed kinase inhibitor beads by gravity (Sepharose conjugated to VI-16832, CTx-0294885, PP58, Purvalanol B, UNC8088A, and UNC21474). Beads were washed first with high salt (1 M

NaCl) followed by low salt (150 mM NaCl + 0.1% SDS) buffers. Kinases were eluted by boiling beads for 5 minutes in elution buffer (100 mM Tris-HCl [pH 6.8], 0.5% SDS, 1% β-mercaptoethanol). Eluted kinases were reduced (dithiothreitol) and alkylated (iodoacetamide) before concentration with 10 kD MWCO (Amicon Ultra-4) and subsequent chloroform/methanol extraction. Protein pellets were resuspended (50 mM HEPES, pH 8.0) and digested with sequencing grade trypsin (Promega) overnight at 37^{O}C. Peptides were purified using PepClean C18 Spin Columns (Thermo Scientific).

Kinome LC/MS/MS and data analysis

Purified peptides were analyzed by LC/MS/MS by an Easy nLC 1000 coupled to a Qexactive HF mass spectrometer (Thermo Scientific) operated in data-dependent mode using the top 15 ions. Peptides were separated by an Easy Spray PrepMap C18 column (75 μm × 25 cm × 2 μm particles; Thermo Scientific) in water with 0.1% formic acid subjected to gradient separation of 5–32% Acetonitrile with 0.1% formic acid at 250 nl/min for 2 hours. Precursor resolution (m/z 400–1600) was set to 120,000 with a target of 3×10^{6} ions and normalized collision energy set at 27% for HCD. Peptides with unknown charge or charge of 1 and ≥ 8 were excluded. Raw data files were analyzed in MaxQuant (77) (MQ) version 1.5.3.17 and searched against Uniprot Human Reference Proteome (78) (20,203 sequences, accessed August 2015) and known contaminants in MQ using Andromeda search engine (79). Spectra were matched between runs (2 minutes match window, 20 minutes alignment window). Protease was set to trypsin with up to two missed cleavages with carbamidomethylation of cysteine set as a fixed modification and oxidation of methionine as a variable modification with 1% FDR. Sample analyses were performed in R (4.2.2). LFQ intensities were first filtered for known human kinases annotated in KinHub that had >2 unique razor peptides with a score > 5. Samples were $\log_2$ transformed and median normalized. Sample quality was assessed by principal component analysis and pearson correlation. Proteins not detected in at least 60% of the samples were removed, and protein intensities were median centered by the median in control samples (DMSO treated). Differential expression was performed by linear models for microarray and RNAseq data (LIMMA) (65, 66) using the individual cell lines as a blocking term (67) when considering all cell lines together. Missing data was not imputed.

Sample preparation for proteomics analysis

For ERKi, MIA PaCa-2, PANC-1, HPAC, Panc 10.05, ASPC-1 and SW1990 were treated with either 1 μM SCH772984 or equivalent volume DMSO for 1 or 24 hours. For G12Ci, H358, SW837, and MIA PaCa-2 cells were treated with either 20 nM MRTX1257 or equivalent DMSO for 24 or 72 hours. For RASi, K8484 cells were treated with either 10 nM RMC-7977 or equivalent DMSO for 24 hours. Cell lysates were prepared in 400–450 μL of lysis buffer (8 M urea, 50 mM NH4HCO3 (pH 7.5), 1x protease inhibitor cocktails (Roche) and 1x phosphatase inhibitor cocktails I and II (Sigma-Aldrich)). Lysates were sonicated six times (15 seconds at 30% frequency, 90 seconds on ice). Following sonication, samples were centrifuged for 10 minutes at 14,000 RPM at 4°C. Supernatants were then passed through a 0.2 μm filter before cryostorage at −80°C. Cell lysates were submitted to the UNC Proteomics Core for additional preparation.

Cell lysates (1 mg per sample) were reduced with 5 mM DTT (45 minutes at 37°C) and alkylated with iodoacetamide (15 mM for 30 minutes in the dark at room temperature). Protein was precipitated at a 1:10 ratio with cold methanol. Precipitates were centrifuged at 5000 rpm at 4°C for 45 minutes and protein pellets were reconstituted in 50 mM ammonium bicarbonate pH 8 to achieve a 0.5 mg/ml concentration. Samples were digested with LysC (Wako, 1:75 w/w) for 2 hours at 37°C, then digested with trypsin (Promega, 1:75 w/w) overnight at 37°C. The resulting peptide samples were acidified, desalted using desalting spin columns (Thermo), then the eluates were dried via vacuum centrifugation. Peptide concentration was determined using Quantitative Colorimetric Peptide Assay (Pierce).

For ERKi and RASi treated cells, 16 total samples per cell line were labeled with TMTpro 16plex reagents (Thermo Fisher). For G12Ci treated cells, ten samples were labeled with TMTpro 10plex reagents (Thermo Fisher). Each sample (125 μg ERKi/G12Ci, 200 μg RASi) was reconstituted with 50 mM HEPES pH 8.5, then individually labeled with TMTpro reagent (250 μg ERKi/G12Ci, 500 μg RASi) for 1 hour at room temperature. Labeling efficiency was evaluated by LC-MS/MS analysis of a pooled sample consisting of 1 μl of each sample. After confirming >98% efficiency, samples were quenched with 50% hydroxylamine to a final concentration of 0.4%. Labeled peptide samples were combined 1:1, desalted using Thermo desalting spin columns, and dried via vacuum centrifugation. The dried TMT-labeled samples were fractionated using high pH reversed phase HPLC (30). Briefly, the samples were offline fractionated into 96 fractions over a 90 minute run by high pH reverse-phase HPLC (Agilent 1260) using an Agilent ZORBAX 300Extend-C18 column (3.5-μm, 4.6 × 250 mm) with mobile phase A containing 4.5 mM ammonium formate (pH 10) in 2% (vol/vol) LC-MS grade acetonitrile, and mobile phase B containing 4.5 mM ammonium formate (pH 10) in 90% (vol/vol) LC-MS grade acetonitrile. The 96 resulting fractions were then concatenated in a non-continuous manner into 24 fractions and 5% of each was aliquotted, dried down via vacuum centrifugation and stored at −80°C until further analysis.

The remaining 95% of each fraction was further concatenated into four fractions and dried down via vacuum centrifugation. For each fraction, phosphopeptides were enriched using the High Select Fe-NTA kit (Thermo). For ERKi and G12Ci treated samples, flow-through was enriched a second time using the High Select TiO_2 kit (Thermo). Manufacturer protocols were followed for both enrichments. Fe-NTA and TiO_2 eluates were dried down via vacuum centrifugation and stored at −80°C until further analysis.

LC/MS/MS analysis

The proteome fractions and phosphoproteome fractions (FeNTA and TiO_2 eluates) for ERKi and G12Ci treated samples were analyzed by LC/MS/MS using an Easy nLC 1200 coupled to an Orbitrap Fusion Lumos Tribrid mass spectrometer (Thermo Scientific). The proteome and phosphoproteome fractions (FeNTA eluates) for RASi treated samples were analyzed by LC/MS/MS using a Thermo Ultimate3000 nanoLC coupled to an Exploris480 mass spectrometer (Thermo Scientific). ERKi/G12Ci treated samples were injected onto an Easy Spray PepMap C18 column (75 μm id × 25 cm, 2 μm particle size) (Thermo Scientific) and separated over 120 minutes. The gradient for separation consisted of 5–42% mobile

phase B at a 250 nl/minute flow rate, where mobile phase A was 0.1% formic acid in water and mobile phase B consisted of 0.1% formic acid in 80% ACN. RASi treated samples were injected onto an Ion Opticks Aurora C18 column (75 μm id × 15 cm, 1.6 μm particle size) and separated over 70 or 100 minutes. The gradient for separation consisted of 5–42% mobile phase B at a 250 nl/minute flow rate, where mobile phase A was 0.1% formic acid in water and mobile phase B consisted of 0.1% formic acid in 80% ACN.

For the ERKi proteome fractions, the Lumos was operated in SPS-MS3 mode (80), with a 3 sec cycle time. Resolution for the precursor scan (m/z 400–1500) was set to 120,000 with an AGC target set to standard and a maximum injection time of 50 milliseconds. MS2 scans consisted of CID normalized collision energy (NCE) 32; AGC target set to standard; maximum injection time of 50 milliseconds; isolation window of 0.7 Da. Following MS2 acquisition, MS3 spectra were collected in SPS mode (10 scans per outcome); HCD set to 55; resolution set to 50,000; scan range set to 100–500; AGC target set to 200% with a 100 milliseconds maximum inject time.

For the phosphoproteome fractions, the Lumos was operated in MS2 mode (28, 29) with a 3-second cycle time. Resolution for the precursor scan (m/z 400–1500) was set to 60,000 with a AGC target set to standard and a maximum injection time of 50 milliseconds. For MS2 scans, HCD was set to 35; AGC target set to 200%; maximum injection time of 120 milliseconds; isolation window of 0.7 Da; resolution set to 50,000. The Exploris480 was operated in turboTMTpro mode with a cycle time of 3 seconds. Resolution for the precursor scan (m/z 375–1400) was set to 60,000 with an AGC target set to standard and a maximum injection time set to auto. MS2 scans (30,000 resolution) consisted of higher collision dissociate (HCD) set to 38; AGC target set to 300%; maximum injection time set to auto; isolation window of 0.7 Da; fixed first mass of 110 m/z.

Proteomics MS search

All MS raw files were jointly searched by treatment condition (ERKi/G12Ci/RASi) using the MaxQuant (77) (MQ) 2.4.3.0 Andromeda search engine (79) and the UniProt Human Reference Proteome (78) (20,586 sequences, accessed August 2023) for ERKi/G12Ci treated samples or Uniprot Mouse Reference Proteome (21,864 sequences, accessed October 2023) for RASi treated samples, and known contaminants included in MQ. The peptide length was set to 8–25 with a maximum mass of 4,600 Da. False Discovery Rate (FDR) for peptide identification was set at <0.01 with a minimum of one razor peptide. Peptide search was matched between runs with a match time window of 0.7 min.

For identification of modified peptides, MS2 reporter ion for TMTpro-16plex or 10plex (Thermo) was searched using manufacturer’s isotope correction factors with a reporter mass tolerance of 0.003 Da. Reporter ions were filtered by a minimum precursor intensity fraction (PIF) of 0.75. Oxidation, N-terminal acetylation, and phospho-serine/threonine/tyrosine (STY) were set as variable modifications, and carbamidomethyl was set as fixed modifications with a maximum number of five modifications per peptide. Digestion was set to Trypsin/P with three maximum missed cleavages. Default orbitrap settings were used for spectrometer.

To reduce ratio compression for global proteomics (81), unmodified peptides were searched by MS3 reporter ion for TMTpro-16plex (Thermo) using manufacturer's isotope correction factors and mass tolerance of 0.003 Da. Oxidation and N-terminal acetylation were set as variable modifications, and carbamidomethyl was set as fixed modifications. All other settings were the same as for modified peptide search.

Proteomics differential expression analysis

Global proteomic and phosphoproteomic differential expression analysis was performed in R (v4.2.2) using LIMMA (65). Contaminants and reverse sequences were removed, and sample intensities were $\log_2$ transformed and median normalized. Sample quality was assessed by total intensity distributions, principal component analysis, and sample correlation analyses. For phosphoproteomics samples, phosphosites were filtered for Class I phosphosite assignment (localization probability > 75%). Proteins and phosphosites were median centered by the median of control samples (DMSO) before performing differential expression analysis (66). When considering all cell lines together, individual cell lines were used as a blocking term (67). Missing data was not imputed.

Database comparisons

The CPTAC PDA dataset was prepared using Supplemental Table S3 from Cao *et al.* (2021) (26) with reported differential expression of phosphosites in tumors versus non-adjacent normal tissues. Differentially regulated phosphosites were defined as having a false-discovery rate of <0.05. The ERK Compendium dataset was prepared from Unal *et al.* (2017) (21). The databases of known regulatory sites, phosphosites with Cell Signaling Technologies antibodies, and all annotated PSP phosphosites were prepared from PhosphoSitePlus (25) and filtered for human phosphosites. The post-translational modification signature database (PTMsigDB) dataset was prepared by downloading the human PTMsigDB set (v1.9.0) (82). The functional human phosphoproteome was prepared from Supplementary Table S43 from Ochoa *et al.* (2019) (27). A database of annotated human kinases was prepared from KinHub. Transcription factors were annotated from Supplemental Table S1 from Lambert *et al.* (2018) (83) and filtered for transcription factors. Protein phosphatases were annotated from Supplemental Table S1 from Chen *et al.* (2017) (84) and filtered for proteins within the evolutionarily conserved human protein phosphatome. A catalogue of E3 ubiquitin ligases was prepared from UbiNet 2.0 (85). Epigenetic regulators were annotated as published in EpiFactors (86, 87). Proteins involved in epigenetic regulation contain proteins annotated to be kinases, transcription factors, phosphatases, or ubiquitin E3 ligases, and these proteins were filtered out of the epigenetic dataset. Other than the epigenetic regulators, other protein groups were found to be mutually exclusive. The membership of each phosphosite or phosphoprotein within each of these datasets was annotated in phosphoproteomics data and used for further analysis.

Human-mouse phosphosite alignment

Gene names of phosphoproteins were converted from human to mouse homologues using msigdbr (v7.5.1). Gene names were matched to the FASTA names in the Uniprot Mouse Reference Proteome (21,864 sequences, accessed October 2023). Each 15-amino acid flanking sequence identified on each phosphoprotein was aligned to the full protein amino

acid sequence of the corresponding mouse homologue using the ClustalOmega method in the multiple sequence alignment (msa) package (v1.32.0) (88). Pairwise distances of the two aligned sequences were computed using seqinr (v4.2–36) (89) to assign an alignment score.

Subcellular localization and motif analyses

Assignment of subcellular localization of proteins was determined by the max score reported by Binder *et al.* (2014)(90) for main subcellular compartments (nucleus, cytoplasm, mitochondrion, lysosome, plasma membrane, cytoskeleton, endosome, peroxisome, and Golgi apparatus).

D motifs were determined by the greater MEF2A D motifs reported in Supplementary Table 1 of Zeke *et al.* (2015) (91) with the addition of RPS6 kinases RPS6KA1–6 and RPS6KB1–2. DEF motifs were identified by regular expression search within the amino acid sequence of each uniprot ID for the amino acid pattern [F/W]-X-[F/W/Y]-P where X is any amino acid.

Overrepresentation was determined by one-tailed hypergeometric testing using all detected phosphosites/phosphoproteins at each respective timepoint as the background, and p values adjusted by the Benjamini-Hochberg procedure. Enrichment was determined by the relative proportion detected in the foreground to the proportion detected in the background.

Phosphoprotein enrichment and network analyses

Gene sets were downloaded from the Molecular Signatures Database (V7.4) and filtered for Reactome gene sets. Overrepresentation was determined by one-tailed hypergeometric testing and p values adjusted by Benjamini-Hochberg with a minimum background set to five phosphoproteins. Enrichment was determined by the relative proportion of representation in the foreground to the proportion in the background. Networks were generated in R (v4.2.2) using the top ten significantly enriched gene sets. Phosphoproteins with differentially regulated phosphosites ($p < 0.05$) and gene sets were defined as the nodes, and edges were defined as the membership of each phosphoprotein within the gene sets.

Phosphatase enrichment analysis

Phosphatase substrates were determined using data from BioGRID (v4.4.213) by filtering for human interactions from annotated phosphatases that have activity towards protein substrates. Differentially regulated phosphosites were used to determine proteins with down or upregulated phosphosites ($p<0.01$). Phosphatase activity enrichment was determined by comparing enrichment of phosphatase substrates with down or upregulated phosphosites (foreground) to all phosphatase substrates detected (background) using one-tailed hypergeometric testing with p values adjusted by Benjamini-Hochberg. Only phosphatases with a minimum of 20 substrates detected were considered.

Kinase library analysis and network construction

Differentially regulated phosphosites were analyzed for kinase motif enrichment as reported previously (37). Relative kinase activities were determined by the product min-max

normalized adjusted p values and $\log_2$ enrichment factor for the most significant enrichment direction for each kinase. Individual phosphosites were scored for the 303 human kinases as described previously (37), and top kinases for phosphosites were filtered for the top 25 scoring kinases by percentile. The first kinase-phosphosite link was assigned a score by taking the product of the kinase-phosphosite percentile and absolute value of the relative kinase activities for each cell line and comparison and defined as the kinase library score. Previously reported kinase-phosphosite evidence was added to the kinase library score by integrating the kinase-substrate dataset available from PhosphoSitePlus (25). A score of 0.5 was added to the kinase library score for each level of evidence, *in vitro* and *in vivo*, reported in the kinase-substrate set. Because the kinase library does not assign a kinase to phospho-tyrosine sites, the link for phospho-tyrosines was created by the evidence within the PSP kinase-substrate dataset. The PSP score was added to the kinase library score.

Next, kinase-substrate interactions were annotated from the PhosphoNetworks (38) and BioGRID (39) databases. Kinase-substrate interactions from PhosphoNetworks were assigned a score of 0.5 and added to the kinase library score. Data from BioGRID (v4.4.213) was filtered for human interactions and the score was scaled by the number of references that reported the kinase-substrate interaction (score = n/[n+1], where n is the number of references reporting the interaction). The BioGRID score for each kinase-substrate interaction was added to the kinase library score.

The final interaction score was determined by taking the product of the final kinase library score and the relative phosphosite differential regulation matched for each cell line and comparison. The relative phosphosite differential regulation was calculated by the product of the min-max normalized adjusted p values and $\log_2$ fold-change for each cell line and comparison. Each phosphosite was filtered for the top three kinase interaction scores. This score represents the likelihood that a kinase is responsible for regulating that individual phosphosite. The final kinase interaction score for kinase-substrate interactions was defined as the sum of interaction scores for each phosphosite. All computations were performed in R (v4.2.2) and networks were created using the final interaction score for each kinase-substrate as links and each kinase and substrate as nodes. Nodes were annotated by databases as described above.

Kinase tree

Relative kinase activities were plotted in Coral (92) using relative activities described above as node size, branch color, and node color.

Motif analyses

Flanking sequences for the background detected sequences were annotated as position specific frequency matrices (PSFMs). Foreground sequences were determined for indicated kinases by filtering for kinase interactions defined in the kinase-substrate network defined above. Flanking sequences for phosphosites attributed to the indicated kinase within the kinase-substrate network were annotated as PSFMs. Enrichment or depletion was determined by subtracting the foreground PSFM by the background PSFM. Motifs were

visualized using the R package ggseqlogo (93) using the determined enrichment/depletion values.

DepMap analyses

Data from DepMap (22Q1) was accessed through ExperimentHub (94). CRISPR Chronos dependency data (EH7523) and cell line mutation calls (EH7526) were retrieved. Mutation calls were used to annotate KRAS mutant status for each cell line, where the amino acid substitutions G12A, G12C, G12D, G12R, G12S, G12V, G13D, Q61H, Q61K, Q61L, or Q61R were considered as KRAS mutant.

Foreground for overrepresentation analyses of ERK regulated phosphoproteins was determined for proteins with median Chronos dependency < −0.5 of the 43 KRAS mutant PDAC cell lines. Annotated protein localizations and gene set memberships were defined as described above. Overrepresentation was determined by one-tailed hypergeometric testing using the background of all detected phosphoproteins.

KRAS mutant select genetic dependencies were determined by a two-way ANOVA of Chronos dependency versus KRAS mutation status and cancer type. Cancer types included in these analyses were defined as having at least 10% KRAS mutant cell lines. The Tukey Honestly Significant Difference (HSD) post hoc test was used to determine statistical significance.

Statistics and reproducibility

The data are represented as described in the figure legends. The number of technical or biological replicates, fields of images used for analysis, statistical cut-offs used to present data, and statistical tests are described in the figure legends and corresponding materials and methods sections. When appropriate, p values were adjusted for multiple hypothesis testing as described in the Figure Legends and Materials and Methods.

Supplementary Material

Refer to Web version on PubMed Central for supplementary material.

ACKNOWLEDGEMENTS

We thank J. Zhang (UCSD) for EKAR4 plasmids, Revolution Medicines for providing the RAS(ON) multi-selective tri-complex inhibitor (RMC-7797), A. Maitra (MD Anderson Cancer Center) and K. P. Olive (Columbia University) for providing cell lines.

Funding:

National Cancer Institute grants R01CA42978, P50CA196510, P50CA257911, U01CA199235, P01CA203657 and R35CA232113 (A.D.C. and/or C.J.D.)

Pancreatic Cancer Action Network grant 22-WG-DERB (C.J.D.)

Department of Defense grant W81XWH2110692 (C.J.D.)

Lustgarten Foundation grant 388222 (C.J.D.)

National Cancer Institute grant R35CA197588 (L.C.C.)

Pancreatic Cancer Action Network/AACR grant 15-70-25-BRYA (K.L.B.)

National Cancer Institute grants P50CA196510 and R37CA251877 (K.L.B.)

Department of Defense grant W81XWH2110693 (K.L.B.)

Sky Foundation grant (K.L.B.)

National Institute of General Medical Sciences grant R01GM138520 (L.M.G.)

National Cancer Institute grants T32CA009156, F32CA23932, and K99CA276700 (J.E.K.)

American Cancer Society grant PF-20-069 (J.E.K.)

Slomo and Cindy Silvian Foundation (J.N.D.)

National Cancer Institute grants T32CA071341 and F30CA243253) (J.N.D.)

National Institute of General Medical Sciences grant T32GM119999 (A.C.E.)

National Cancer Institute grant F31CA275260 (A.C.E.)

National Cancer Institute grant T32CA009156 (K.D.M.)

American Cancer Society grant PF-22-066-01-TBE (K.D.M.)

National Cancer Institute grants T32CA009156 and F32CA232529 (C.A.S.)

This research is based in part upon work conducted using the UNC Proteomics Core Facility, which is supported in part by P30 CA016086 Cancer Center Core Support Grant to the UNC Lineberger Comprehensive Cancer Center.

Competing interests:

C.J.D. was a consultant/advisory board member for Cullgen, Deciphera Pharmaceuticals, Kestrel Therapeutics, Mirati Therapeutics, Reactive Biosciences, Revere Pharmaceuticals, Revolution Medicines Ribometrics, Sanofi and SHY Therapeutics. C.J.D. has received research funding support from Deciphera Pharmaceuticals, Mirati Therapeutics, Reactive Biosciences, Revolution Medicines, and SpringWorks Therapeutics. A.D.C. has consulted for Eli Lilly and Mirati Therapeutics. M.P. and E.F.P. receive royalties from and are consultants of TheraLink Technologies, Inc. K.L.B. has received research funding support from SpringWorks Therapeutics. E.F.P. is a shareholder and consultant of Avant Diagnostics, TheraLink Technologies, Inc. and Perthera, E.F.P. received funding support from Mirati Therapeutics, Genentech, Inc., and Abbvie, Inc. C.A.S. has received consulting fees from Reactive Biosciences. L.C.C. is a founder and member of the board of directors of Agios Pharmaceuticals and is a founder and receives research support from Petra Pharmaceuticals; is listed as an inventor on a patent (WO2019232403A1, Weill Cornell Medicine) for combination therapy for PI3K-associated disease or disorder, and the identification of therapeutic interventions to improve response to PI3K inhibitors for cancer treatment; is a co-founder and shareholder in Faeth Therapeutics; has equity in and consults for Cell Signaling Technologies, Volastra, Larkspur and 1 Base Pharmaceuticals; and consults for Loxo-Lilly. T.M.Y. is a co-founder and stockholder and is on the board of directors of DESTROKE, an early-stage start-up developing mobile technology for automated clinical stroke detection. J.L.J. has received consulting fees from Scorpion Therapeutics and Volastra Therapeutics. The other authors declare no competing interests.

DATA AND MATERIALS AVAILABILITY

All data supporting the findings in this study are provided in the paper or supplementary materials, or deposited in public repositories as described below. Methods of analysis needed to reproduce these observations are described in Materials and Methods. Requests for materials related to this study should be addressed to CAS. Novel plasmids can be found on Addgene using the ID numbers listed in Materials and Methods. MIB/MS, phosphoproteomic and global proteomic data have been deposited to the ProteomeXchange Consortium via the PRIDE partner repository. ERKi MIB/MS data are available with identifier PXD043585, and phosphoproteomic and global proteomic data are available with

the identifiers PXD048529 (10.6019/PXD048529), and PXD048531 (10.6019/PXD048531). G12Ci and RASi phosphoproteomic data are available with identifiers PXD048532 (10.6019/PXD048532) and PXD048534 (10.6019/PXD048534). The RNA-seq data used in this study have been deposited to the NCBI Sequence Read Archives (SRA) (ERK1/2^{SD} with KRASi, PRJNA1056120) or have been published previously (31) (ERKi time series, NCBI SRA PRJEB25806).

REFERENCES AND NOTES

1. Hayashi A, Hong J, Iacobuzio-Donahue CA, The pancreatic cancer genome revisited. Nat. Rev. Gastroenterol. Hepatol 18, 469–481 (2021). [PubMed: 34089011]
2. Drosten M, Barbacid M, Targeting the MAPK Pathway in KRAS-Driven Tumors. Cancer Cell 37, 543–550 (2020). [PubMed: 32289276]
3. Karoulia Z, Gavathiotis E, Poulikakos PI, New perspectives for targeting RAF kinase in human cancer. Nat. Rev. Cancer 17, 676–691 (2017). [PubMed: 28984291]
4. Terrell EM, Morrison DK, Ras-Mediated Activation of the Raf Family Kinases. Cold Spring Harb. Perspect. Med 9 (2019).
5. Klomp JE, Klomp JA, Der CJ, The ERK mitogen-activated protein kinase signaling network: the final frontier in RAS signal transduction. Biochem. Soc. Trans 49, 253–267 (2021). [PubMed: 33544118]
6. Lavoie H, Gagnon J, Therrien M, ERK signalling: a master regulator of cell behaviour, life and fate. Nat. Rev. Mol. Cell Biol 21, 607–632 (2020). [PubMed: 32576977]
7. Klomp JA, Klomp JE, Stalnecker CA, Bryant KL, Edwards AC, Drizyte-Miller K, Hibshman PS, Diehl JN, Lee YS, Morales AJ, Taylor KE, Peng S, Tran NL, Herring LE, Prevatte AW, Barker NK, Hover LD, Hallin J, Chowdhury S, Coker O, Lee HM, Goodwin CM, Gautam P, Olson P, Christensen JG, Shen JP, Kopetz S, Graves LM, Lim K-H, Wang-Gillam A, Wennerberg K, Cox AD, Der CJ, Defining the KRAS-Dependent Transcriptome in KRAS-Mutant Pancreatic Cancer. Sci. Revis
8. Liberzon A, Birger C, Thorvaldsdóttir H, Ghandi M, Mesirov JP, Tamayo P, The Molecular Signatures Database (MSigDB) hallmark gene set collection. Cell Syst. 1, 417–425 (2015). [PubMed: 26771021]
9. Smorodinsky-Atias K, Goshen-Lago T, Goldberg-Carp A, Melamed D, Shir A, Mooshayef N, Beenstock J, Karamansha Y, Darlyuk-Saadon I, Livnah O, Ahn NG, Admon A, Engelberg D, Intrinsically active variants of Erk oncogenically transform cells and disclose unexpected autophosphorylation capability that is independent of TEY phosphorylation. Mol. Biol. Cell 27, 1026–1039 (2016). [PubMed: 26658610]
10. Emrick MA, Hoofnagle AN, Miller AS, Ten Eyck LF, Ahn NG, Constitutive activation of extracellular signal-regulated kinase 2 by synergistic point mutations. J. Biol. Chem 276, 46469–46479 (2001). [PubMed: 11591711]
11. Smorodinsky-Atias K, Soudah N, Engelberg D, Mutations That Confer Drug-Resistance, Oncogenicity and Intrinsic Activity on the ERK MAP Kinases-Current State of the Art. Cells 9, 129 (2020). [PubMed: 31935908]
12. Sun X-X, Li Y, Sears RC, Dai M-S, Targeting the MYC Ubiquitination-Proteasome Degradation Pathway for Cancer Therapy. Front. Oncol 11, 679445 (2021). [PubMed: 34178666]
13. Fell JB, Fischer JP, Baer BR, Blake JF, Bouhana K, Briere DM, Brown KD, Burgess LE, Burns AC, Burkard MR, Chiang H, Chicarelli MJ, Cook AW, Gaudino JJ, Hallin J, Hanson L, Hartley DP, Hicken EJ, Hingorani GP, Hinklin RJ, Mejia MJ, Olson P, Otten JN, Rhodes SP, Rodriguez ME, Savechenkov P, Smith DJ, Sudhakar N, Sullivan FX, Tang TP, Vigers GP, Wollenberg L, Christensen JG, Marx MA, Identification of the Clinical Development Candidate MRTX849, a Covalent KRASG12C Inhibitor for the Treatment of Cancer. J. Med. Chem 63, 6679–6693 (2020). [PubMed: 32250617]
14. Wang X, Allen S, Blake JF, Bowcut V, Briere DM, Calinisan A, Dahlke JR, Fell JB, Fischer JP, Gunn RJ, Hallin J, Laguer J, Lawson JD, Medwid J, Newhouse B, Nguyen P, O'Leary JM, Olson

P, Pajk S, Rahbaek L, Rodriguez M, Smith CR, Tang TP, Thomas NC, Vanderpool D, Vigers GP, Christensen JG, Marx MA, Identification of MRTX1133, a Noncovalent, Potent, and Selective KRASG12D Inhibitor. J. Med. Chem 65, 3123–3133 (2022). [PubMed: 34889605]

15. Waters AM, Der CJ, KRAS: The Critical Driver and Therapeutic Target for Pancreatic Cancer. Cold Spring Harb. Perspect. Med 8, a031435 (2018). [PubMed: 29229669]
16. Collisson EA, Trejo CL, Silva JM, Gu S, Korkola JE, Heiser LM, Charles R-P, Rabinovich BA, Hann B, Dankort D, Spellman PT, Phillips WA, Gray JW, McMahon M, A central role for RAF→MEK→ERK signaling in the genesis of pancreatic ductal adenocarcinoma. Cancer Discov. 2, 685–693 (2012). [PubMed: 22628411]
17. Smith MJ, Ikura M, Integrated RAS signaling defined by parallel NMR detection of effectors and regulators. Nat. Chem. Biol 10, 223–230 (2014). [PubMed: 24441586]
18. Kiel C, Foglierini M, Kuemmerer N, Beltrao P, Serrano L, A genome-wide Ras-effector interaction network. J. Mol. Biol 370, 1020–1032 (2007). [PubMed: 17544445]
19. Catozzi S, Halasz M, Kiel C, Predicted “wiring landscape” of Ras-effector interactions in 29 human tissues. NPJ Syst. Biol. Appl 7, 10 (2021). [PubMed: 33580066]
20. Saba-El-Leil MK, Frémin C, Meloche S, Redundancy in the World of MAP Kinases: All for One. Front. Cell Dev. Biol 4, 67 (2016). [PubMed: 27446918]
21. Ünal EB, Uhlitz F, Blüthgen N, A compendium of ERK targets. FEBS Lett. 591, 2607–2615 (2017). [PubMed: 28675784]
22. Yoon S, Seger R, The extracellular signal-regulated kinase: Multiple substrates regulate diverse cellular functions. Growth Factors 24, 21–44 (2006). [PubMed: 16393692]
23. Duncan JS, Whittle MC, Nakamura K, Abell AN, Midland AA, Zawistowski JS, Johnson NL, Granger DA, Jordan NV, Darr DB, Usary J, Kuan P-F, Smalley DM, Major B, He X, Hoadley KA, Zhou B, Sharpless NE, Perou CM, Kim WY, Gomez SM, Chen X, Jin J, Frye SV, Earp HS, Graves LM, Johnson GL, Dynamic Reprogramming of the Kinome In Response to Targeted MEK Inhibition In Triple Negative Breast Cancer. Cell 149, 307–321 (2012). [PubMed: 22500798]
24. Klaeger S, Heinzlmeir S, Wilhelm M, Polzer H, Vick B, Koenig P-A, Reinecke M, Ruprecht B, Petzoldt S, Meng C, Zecha J, Reiter K, Qiao H, Helm D, Koch H, Schoof M, Canevari G, Casale E, Depaolini SR, Feuchtinger A, Wu Z, Schmidt T, Rueckert L, Becker W, Huenges J, Garz A-K, Gohlke B-O, Zolg DP, Kayser G, Vooder T, Preissner R, Hahne H, Tõnisson N, Kramer K, Götze K, Bassermann F, Schlegl J, Ehrlich H-C, Aiche S, Walch A, Greif PA, Schneider S, Felder ER, Ruland J, Médard G, Jeremias I, Spiekermann K, Kuster B, The target landscape of clinical kinase drugs. Science 358, eaan4368 (2017). [PubMed: 29191878]
25. Hornbeck PV, Zhang B, Murray B, Kornhauser JM, Latham V, Skrzypek E, PhosphoSitePlus, 2014: mutations, PTMs and recalibrations. Nucleic Acids Res. 43, 512–520 (2015).
26. Cao L, Huang C, Cui Zhou D, Hu Y, Lih TM, Savage SR, Krug K, Clark DJ, Schnaubelt M, Chen L, da Veiga Leprevost F, Eguez RV, Yang W, Pan J, Wen B, Dou Y, Jiang W, Liao Y, Shi Z, Terekhanova NV, Cao S, Lu RJ-H, Li Y, Liu R, Zhu H, Ronning P, Wu Y, Wyczalkowski MA, Easwaran H, Danilova L, Mer AS, Yoo S, Wang JM, Liu W, Haibe-Kains B, Thiagarajan M, Jewell SD, Hostetter G, Newton CJ, Li QK, Roehrl MH, Fenyö D, Wang P, Nesvizhskii AI, Mani DR, Omenn GS, Boja ES, Mesri M, Robles AI, Rodriguez H, Bathe OF, Chan DW, Hruban RH, Ding L, Zhang B, Zhang H, Clinical Proteomic Tumor Analysis Consortium, Proteogenomic characterization of pancreatic ductal adenocarcinoma. Cell 184, 5031–5052 (2021). [PubMed: 34534465]
27. Ochoa D, Jarnuczak AF, Viéitez C, Gehre M, Soucheray M, Mateus A, Kleefeldt AA, Hill A, Garcia-Alonso L, Stein F, Krogan NJ, Savitski MM, Swaney DL, Vizcaíno JA, Noh K-M, Beltrao P, The functional landscape of the human phosphoproteome. Nat. Biotechnol 38, 365–373 (2020). [PubMed: 31819260]
28. Hogrebe A, von Stechow L, Bekker-Jensen DB, Weinert BT, Kelstrup CD, Olsen JV, Benchmarking common quantification strategies for large-scale phosphoproteomics. Nat. Commun 9, 1045 (2018). [PubMed: 29535314]
29. Klann K, Bojkova D, Tascher G, Ciesek S, Münch C, Cinatl J, Growth Factor Receptor Signaling Inhibition Prevents SARS-CoV-2 Replication. Mol. Cell 80, 164–174 (2020). [PubMed: 32877642]

30. Mertins P, Tang LC, Krug K, Clark DJ, Gritsenko MA, Chen L, Clauser KR, Clauss TR, Shah P, Gillette MA, Petyuk VA, Thomas SN, Mani DR, Mundt F, Moore RJ, Hu Y, Zhao R, Schnaubelt M, Keshishian H, Monroe ME, Zhang Z, Udeshi ND, Mani D, Davies SR, Townsend RR, Chan DW, Smith RD, Zhang H, Liu T, Carr SA, Reproducible workflow for multiplexed deep-scale proteome and phosphoproteome analysis of tumor tissues by liquid chromatography-mass spectrometry. Nat. Protoc 13, 1632–1661 (2018). [PubMed: 29988108]

31. Bryant KL, Stalnecker CA, Zeitouni D, Klomp JE, Peng S, Tikunov AP, Gunda V, Pierobon M, Waters AM, George SD, Tomar G, Papke B, Hobbs GA, Yan L, Hayes TK, Diehl JN, Goode GD, Chaika NV, Wang Y, Zhang G-F, Witkiewicz AK, Knudsen ES, Petricoin EF, Singh PK, Macdonald JM, Tran NL, Lyssiotis CA, Ying H, Kimmelman AC, Cox AD, Der CJ, Combination of ERK and autophagy inhibition as a treatment approach for pancreatic cancer. Nat. Med 25, 628–640 (2019). [PubMed: 30833752]

32. Holderfield M, Lee BJ, Jiang J, Tomlinson A, Seamon KJ, Mira A, Patrucco E, Goodhart G, Dilly J, Gindin Y, Dinglasan N, Wang Y, Lai LP, Cai S, Jiang L, Nasholm N, Shifrin N, Blaj C, Shah H, Evans JW, Montazer N, Lai O, Shi J, Ahler E, Quintana E, Chang S, Salvador A, Marquez A, Cregg J, Liu Y, Milin A, Chen A, Ziv TB, Parsons D, Knox JE, Klomp JE, Roth J, Rees M, Ronan M, Cuevas-Navarro A, Hu F, Lito P, Santamaria D, Aguirre AJ, Waters AM, Der CJ, Ambrogio C, Wang Z, Gill AL, Koltun ES, Smith JAM, Wildes D, Singh M, Concurrent inhibition of oncogenic and wild-type RAS-GTP for cancer therapy. Nature, doi: 10.1038/s41586-024-07205-6 (2024).

33. Gonzalez FA, Raden DL, Davis RJ, Identification of substrate recognition determinants for human ERK1 and ERK2 protein kinases. J. Biol. Chem 266, 22159–22163 (1991). [PubMed: 1939237]

34. Futran AS, Link AJ, Seger R, Shvartsman SY, ERK as a model for systems biology of enzyme kinetics in cells. Curr. Biol. CB 23, 972–979 (2013).

35. Keyes J, Ganesan A, Molinar-Inglis O, Hamidzadeh A, Zhang J, Ling M, Trejo J, Levchenko A, Zhang J, Signaling diversity enabled by Rap1-regulated plasma membrane ERK with distinct temporal dynamics. eLife 9, e57410 (2020). [PubMed: 32452765]

36. Dimitri CA, Dowdle W, MacKeigan JP, Blenis J, Murphy LO, Spatially Separate Docking Sites on ERK2 Regulate Distinct Signaling Events In Vivo. Curr. Biol 15, 1319–1324 (2005). [PubMed: 16051177]

37. Johnson JL, Yaron TM, Huntsman EM, Kerelsky A, Song J, Regev A, Lin T-Y, Liberatore K, Cizin DM, Cohen BM, Vasan N, Ma Y, Krismer K, Robles JT, van de Kooij B, van Vlimmeren AE, Andrée-Busch N, Käufer NF, Dorovkov MV, Ryazanov AG, Takagi Y, Kastenhuber ER, Goncalves MD, Hopkins BD, Elemento O, Taatjes DJ, Maucuer A, Yamashita A, Degterev A, Uduman M, Lu J, Landry SD, Zhang B, Cossentino I, Linding R, Blenis J, Hornbeck PV, Turk BE, Yaffe MB, Cantley LC, An atlas of substrate specificities for the human serine/threonine kinome. Nature 613, 759–766 (2023). [PubMed: 36631611]

38. Hu J, Rho H-S, Newman RH, Zhang J, Zhu H, Qian J, PhosphoNetworks: a database for human phosphorylation networks. Bioinforma. Oxf. Engl 30, 141–142 (2014).

39. Oughtred R, Rust J, Chang C, Breitkreutz B-J, Stark C, Willems A, Boucher L, Leung G, Kolas N, Zhang F, Dolma S, Coulombe-Huntington J, Chatr-Aryamontri A, Dolinski K, Tyers M, The BioGRID database: A comprehensive biomedical resource of curated protein, genetic, and chemical interactions. Protein Sci. Publ. Protein Soc 30, 187–200 (2021).

40. Anjum R, Blenis J, The RSK family of kinases: emerging roles in cellular signalling. Nat. Rev. Mol. Cell Biol 9, 747–758 (2008). [PubMed: 18813292]

41. Wood DJ, Endicott JA, Structural insights into the functional diversity of the CDK-cyclin family. Open Biol. 8, 180112 (2018). [PubMed: 30185601]

42. Klomp JE, Lee YS, Goodwin CM, Papke B, Klomp JA, Waters AM, Stalnecker CA, DeLiberty JM, Drizyte-Miller K, Yang R, Diehl JN, Yin HH, Pierobon M, Baldelli E, Ryan MB, Li S, Peterson J, Smith AR, Neal JT, McCormick AK, Kuo CJ, Counter CM, Petricoin EF, Cox AD, Bryant KL, Der CJ, CHK1 protects oncogenic KRAS-expressing cells from DNA damage and is a target for pancreatic cancer treatment. Cell Rep. 37, 110060 (2021). [PubMed: 34852220]

43. Waters AM, Khatib TO, Papke B, Goodwin CM, Hobbs GA, Diehl JN, Yang R, Edwards AC, Walsh KH, Sulahian R, McFarland JM, Kapner KS, Gilbert TSK, Stalnecker CA, Javaid S, Barkovskaya A, Grover KR, Hibshman PS, Blake DR, Schaefer A, Nowak KM, Klomp JE, Hayes TK, Kassner M, Tang N, Tanaseichuk O, Chen K, Zhou Y, Kalkat M, Herring LE, Graves LM,

Penn LZ, Yin HH, Aguirre AJ, Hahn WC, Cox AD, Der CJ, Targeting p130Cas- and microtubule-dependent MYC regulation sensitizes pancreatic cancer to ERK MAPK inhibition. Cell Rep. 35, 109291 (2021). [PubMed: 34192548]

44. Hodge RG, Ridley AJ, Regulating Rho GTPases and their regulators. Nat. Rev. Mol. Cell Biol 17, 496–510 (2016). [PubMed: 27301673]
45. Kapoor A, Yao W, Ying H, Hua S, Liewen A, Wang Q, Zhong Y, Wu C-J, Sadanandam A, Hu B, Chang Q, Chu GC, Al-Khalil R, Jiang S, Xia H, Fletcher-Sananikone E, Lim C, Horwitz GI, Viale A, Pettazzoni P, Sanchez N, Wang H, Protopopov A, Zhang J, Heffernan T, Johnson RL, Chin L, Wang YA, Draetta G, DePinho RA, Yap1 activation enables bypass of oncogenic Kras addiction in pancreatic cancer. Cell 158, 185–197 (2014). [PubMed: 24954535]
46. Shao DD, Xue W, Krall EB, Bhutkar A, Piccioni F, Wang X, Schinzel AC, Sood S, Rosenbluh J, Kim JW, Zwang Y, Roberts TM, Root DE, Jacks T, Hahn WC, KRAS and YAP1 converge to regulate EMT and tumor survival. Cell 158, 171–184 (2014). [PubMed: 24954536]
47. Mukhopadhyay S, Huang H-Y, Lin Z, Ranieri M, Li S, Sahu S, Liu Y, Ban Y, Guidry K, Hu H, Lopez A, Sherman F, Tan YJ, Lee YT, Armstrong AP, Dolgalev I, Sahu P, Zhang T, Lu W, Gray NS, Christensen JG, Tang TT, Velcheti V, Khodadadi-Jamayran A, Wong K-K, Neel BG, Genome-Wide CRISPR Screens Identify Multiple Synthetic Lethal Targets That Enhance KRASG12C Inhibitor Efficacy. Cancer Res. 83, 4095–4111 (2023). [PubMed: 37729426]
48. Edwards AC, Stalnecker CA, Jean Morales A, Taylor KE, Klomp JE, Klomp JA, Waters AM, Sudhakar N, Hallin J, Tang TT, Olson P, Post L, Christensen JG, Cox AD, Der CJ, TEAD Inhibition Overcomes YAP1/TAZ-Driven Primary and Acquired Resistance to KRASG12C Inhibitors. Cancer Res. 83, 4112–4129 (2023). [PubMed: 37934103]
49. Vaseva AV, Blake DR, Gilbert TSK, Ng S, Hostetter G, Azam SH, Ozkan-Dagliyan I, Gautam P, Bryant KL, Pearce KH, Herring LE, Han H, Graves LM, Witkiewicz AK, Knudsen ES, Pecot CV, Rashid N, Houghton PJ, Wennerberg K, Cox AD, Der CJ, KRAS Suppression-Induced Degradation of MYC Is Antagonized by a MEK5-ERK5 Compensatory Mechanism. Cancer Cell 34, 807–822 (2018). [PubMed: 30423298]
50. Bollag G, Hirth P, Tsai J, Zhang J, Ibrahim PN, Cho H, Spevak W, Zhang C, Zhang Y, Habets G, Burton EA, Wong B, Tsang G, West BL, Powell B, Shellooe R, Marimuthu A, Nguyen H, Zhang KYJ, Artis DR, Schlessinger J, Su F, Higgins B, Iyer R, D'Andrea K, Koehler A, Stumm M, Lin PS, Lee RJ, Grippo J, Puzanov I, Kim KB, Ribas A, McArthur GA, Sosman JA, Chapman PB, Flaherty KT, Xu X, Nathanson KL, Nolop K, Clinical efficacy of a RAF inhibitor needs broad target blockade in BRAF-mutant melanoma. Nature 467, 596–599 (2010). [PubMed: 20823850]
51. Herrero A, Pinto A, Colón-Bolea P, Casar B, Jones M, Agudo-Ibáñez L, Vidal R, Tenbaum SP, Nuciforo P, Valdizán EM, Horvath Z, Orfi L, Pineda-Lucena A, Bony E, Keri G, Rivas G, Pazos A, Gozalbes R, Palmer HG, Hurlstone A, Crespo P, Small Molecule Inhibition of ERK Dimerization Prevents Tumorigenesis by RAS-ERK Pathway Oncogenes. Cancer Cell 28, 170–182 (2015). [PubMed: 26267534]
52. Plotnikov A, Flores K, Maik-Rachline G, Zehorai E, Kapri-Pardes E, Berti DA, Hanoch T, Besser MJ, Seger R, The nuclear translocation of ERK1/2 as an anticancer target. Nat. Commun 6, 6685 (2015). [PubMed: 25819065]
53. Vallejo A, Perurena N, Guruceaga E, Mazur PK, Martinez-Canarias S, Zandueta C, Valencia K, Arricibita A, Gwinn D, Sayles LC, Chuang C-H, Guembe L, Bailey P, Chang DK, Biankin A, Ponz-Sarvise M, Andersen JB, Khatri P, Bozec A, Sweet-Cordero EA, Sage J, Lecanda F, Vicent S, An integrative approach unveils FOSL1 as an oncogene vulnerability in KRAS-driven lung and pancreatic cancer. Nat. Commun 8, 14294 (2017). [PubMed: 28220783]
54. Aguirre AJ, Bardeesy N, Sinha M, Lopez L, Tuveson DA, Horner J, Redston MS, DePinho RA, Activated Kras and Ink4a/Arf deficiency cooperate to produce metastatic pancreatic ductal adenocarcinoma. Genes Dev. 17, 3112–3126 (2003). [PubMed: 14681207]
55. Carver J, Dexheimer TS, Hsu D, Weng M-T, Smith JL, Guha R, Jadhav A, Simeonov A, Luo J, A High-Throughput Assay for Small Molecule Destabilizers of the KRAS Oncoprotein. PLOS ONE 9, e103836 (2014). [PubMed: 25093678]
56. Keyes J, Mehta S, Zhang J, Strategies for Multiplexed Biosensor Imaging to Study Intracellular Signaling Networks. Methods Mol. Biol. Clifton NJ 2350, 1–20 (2021).

57. Hobbs GA, Baker NM, Miermont AM, Thurman RD, Pierobon M, Tran TH, Anderson AO, Waters AM, Diehl JN, Papke B, Hodge RG, Klomp JE, Goodwin CM, DeLiberty JM, Wang J, Ng RWS, Gautam P, Bryant KL, Esposito D, Campbell SL, Petricoin EF, Simanshu DK, Aguirre AJ, Wolpin BM, Wennerberg K, Rudloff U, Cox AD, Der CJ, Atypical KRASG12R Mutant Is Impaired in PI3K Signaling and Macropinocytosis in Pancreatic Cancer. Cancer Discov. 10, 104–123 (2020). [PubMed: 31649109]
58. Goodwin CM, Waters AM, Klomp JE, Javaid S, Bryant KL, Stalnecker CA, Drizyte-Miller K, Papke B, Yang R, Amparo AM, Ozkan-Dagliyan I, Baldelli E, Calvert V, Pierobon M, Sorrentino JA, Beelen AP, Bublitz N, Lüthen M, Wood KC, Petricoin EF, Sers C, McRee AJ, Cox AD, Der CJ, Combination Therapies with CDK4/6 Inhibitors to Treat KRAS-mutant Pancreatic Cancer. Cancer Res, CAN-22–0391 (2022).
59. Stalnecker CA, Grover KR, Edwards AC, Coleman MF, Yang R, DeLiberty JM, Papke B, Goodwin CM, Pierobon M, Petricoin EF III, Gautam P, Wennerberg K, Cox AD, Der CJ, Hursting SD, Bryant KL, Concurrent Inhibition of IGF1R and ERK Increases Pancreatic Cancer Sensitivity to Autophagy Inhibitors. Cancer Res. 82, 586–598 (2021).
60. Huynh MV, Hobbs GA, Schaefer A, Pierobon M, Carey LM, Diehl JN, DeLiberty JM, Thurman RD, Cooke AR, Goodwin CM, Cook JH, Lin L, Waters AM, Rashid NU, Petricoin EF, Campbell SL, Haigis KM, Simeone DM, Lyssiotis CA, Cox AD, Der CJ, Functional and biological heterogeneity of KRASQ61 mutations. Sci. Signal 15, eabn2694 (2022). [PubMed: 35944066]
61. Ozkan-Dagliyan I, Diehl JN, George SD, Schaefer A, Papke B, Klotz-Noack K, Waters AM, Goodwin CM, Gautam P, Pierobon M, Peng S, Gilbert TSK, Lin KH, Dagliyan O, Wennerberg K, Petricoin EF, Tran NL, Bhagwat SV, Tiu RV, Peng S-B, Herring LE, Graves LM, Sers C, Wood KC, Cox AD, Der CJ, Low-Dose Vertical Inhibition of the RAF-MEK-ERK Cascade Causes Apoptotic Death of KRAS Mutant Cancers. Cell Rep. 31, 107764 (2020). [PubMed: 32553168]
62. Pierobon M, Ramos C, Wong S, Hodge KA, Aldrich J, Byron S, Anthony SP, Robert NJ, Northfelt DW, Jahanzeb M, Vocila L, Wulfkuhle J, Gambara G, Gallagher RI, Dunetz B, Hoke N, Dong T, Craig DW, Cristofanilli M, Leyland-Jones B, Liotta LA, O'Shaughnessy JA, Carpten JD, Petricoin EF, Enrichment of PI3K-AKT-mTOR Pathway Activation in Hepatic Metastases from Breast Cancer. Clin. Cancer Res. Off. J. Am. Assoc. Cancer Res 23, 4919–4928 (2017).
63. Signore M, Manganelli V, Hodge A, Antibody Validation by Western Blotting. Methods Mol. Biol. Clifton NJ 1606, 51–70 (2017).
64. Pin E, Federici G, Petricoin EF, Preparation and use of reverse protein microarrays. Curr. Protoc. Protein Sci 75, 27.7.1–27.7.29 (2014).
65. Ritchie ME, Phipson B, Wu D, Hu Y, Law CW, Shi W, Smyth GK, limma powers differential expression analyses for RNA-sequencing and microarray studies. Nucleic Acids Res. 43, e47 (2015). [PubMed: 25605792]
66. Phipson B, Lee S, Majewski IJ, Alexander WS, Smyth GK, Robust hyperparameter estimation protects against hypervariable genes and improves power to detect differential expression. Ann. Appl. Stat 10, 946–963 (2016). [PubMed: 28367255]
67. Smyth GK, Michaud J, Scott HS, Use of within-array replicate spots for assessing differential expression in microarray experiments. Bioinformatics 21, 2067–2075 (2005). [PubMed: 15657102]
68. Krueger F, Trim Galore!, version 0.4.1, Babraham Bioinformatics (2012); http://www.bioinformatics.babraham.ac.uk/projects/trim_galore/.
69. Dobin A, Davis CA, Schlesinger F, Drenkow J, Zaleski C, Jha S, Batut P, Chaisson M, Gingeras TR, STAR: ultrafast universal RNA-seq aligner. Bioinformatics 29, 15–21 (2013). [PubMed: 23104886]
70. Frankish A, Diekhans M, Ferreira A-M, Johnson R, Jungreis I, Loveland J, Mudge JM, Sisu C, Wright J, Armstrong J, Barnes I, Berry A, Bignell A, Carbonell Sala S, Chrast J, Cunningham F, Di Domenico T, Donaldson S, Fiddes IT, García Girón C, Gonzalez JM, Grego T, Hardy M, Hourlier T, Hunt T, Izuogu OG, Lagarde J, Martin FJ, Martínez L, Mohanan S, Muir P, Navarro FCP, Parker A, Pei B, Pozo F, Ruffier M, Schmitt BM, Stapleton E, Suner M-M, Sycheva I, Uszczynska-Ratajczak B, Xu J, Yates A, Zerbino D, Zhang Y, Aken B, Choudhary JS, Gerstein M, Guigó R, Hubbard TJP, Kellis M, Paten B, Reymond A, Tress ML, Flicek P, GENCODE

reference annotation for the human and mouse genomes. Nucleic Acids Res. 47, D766–D773 (2019). [PubMed: 30357393]

71. Patro R, Duggal G, Love MI, Irizarry RA, Kingsford C, Salmon provides fast and bias-aware quantification of transcript expression. Nat. Methods 14, 417–419 (2017). [PubMed: 28263959]
72. Soneson C, Love MI, Robinson MD, Differential analyses for RNA-seq: transcript-level estimates improve gene-level inferences. F1000Research 4, 1521 (2015). [PubMed: 26925227]
73. Durinck S, Moreau Y, Kasprzyk A, Davis S, De Moor B, Brazma A, Huber W, BioMart and Bioconductor: a powerful link between biological databases and microarray data analysis. Bioinforma. Oxf. Engl 21, 3439–3440 (2005).
74. Robinson MD, McCarthy DJ, Smyth GK, edgeR: a Bioconductor package for differential expression analysis of digital gene expression data. Bioinformatics 26, 139–140 (2010). [PubMed: 19910308]
75. Robinson MD, Oshlack A, A scaling normalization method for differential expression analysis of RNA-seq data. Genome Biol. 11, R25 (2010). [PubMed: 20196867]
76. Diehl JN, Klomp JE, Snare KR, Hibshman PS, Blake DR, Kaiser ZD, Gilbert TSK, Baldelli E, Pierobon M, Papke B, Yang R, Hodge RG, Rashid NU, Petricoin EF, Herring LE, Graves LM, Cox AD, Der CJ, The KRAS-regulated kinome identifies WEE1 and ERK coinhibition as a potential therapeutic strategy in KRAS-mutant pancreatic cancer. J. Biol. Chem 297, 101335 (2021). [PubMed: 34688654]
77. Cox J, Mann M, MaxQuant enables high peptide identification rates, individualized p.p.b.-range mass accuracies and proteome-wide protein quantification. Nat. Biotechnol 26, 1367–1372 (2008). [PubMed: 19029910]
78. UniProt T Consortium, UniProt: the universal protein knowledgebase. Nucleic Acids Res. 46, 2699 (2018). [PubMed: 29425356]
79. Cox J, Neuhauser N, Michalski A, Scheltema RA, Olsen JV, Mann M, Andromeda: a peptide search engine integrated into the MaxQuant environment. J. Proteome Res 10, 1794–1805 (2011). [PubMed: 21254760]
80. McAlister GC, Nusinow DP, Jedrychowski MP, Wühr M, Huttlin EL, Erickson BK, Rad R, Haas W, Gygi SP, MultiNotch MS3 enables accurate, sensitive, and multiplexed detection of differential expression across cancer cell line proteomes. Anal. Chem 86, 7150–7158 (2014). [PubMed: 24927332]
81. Ting L, Rad R, Gygi SP, Haas W, MS3 eliminates ratio distortion in isobaric multiplexed quantitative proteomics. Nat. Methods 8, 937–940 (2011). [PubMed: 21963607]
82. Krug K, Mertins P, Zhang B, Hornbeck P, Raju R, Ahmad R, Szucs M, Mundt F, Forestier D, Jane-Valbuena J, Keshishian H, Gillette MA, Tamayo P, Mesirov JP, Jaffe JD, Carr S, Mani DR, A Curated Resource for Phosphosite-specific Signature Analysis *[S]. Mol. Cell. Proteomics 18, 576–593 (2019). [PubMed: 30563849]
83. Lambert SA, Jolma A, Campitelli LF, Das PK, Yin Y, Albu M, Chen X, Taipale J, Hughes TR, Weirauch MT, The Human Transcription Factors. Cell 172, 650–665 (2018). [PubMed: 29425488]
84. Chen MJ, Dixon JE, Manning G, Genomics and evolution of protein phosphatases. Sci. Signal 10, eaag1796 (2017). [PubMed: 28400531]
85. Li Z, Chen S, Jhong J-H, Pang Y, Huang K-Y, Li S, Lee T-Y, UbiNet 2.0: a verified, classified, annotated and updated database of E3 ubiquitin ligase-substrate interactions. Database J. Biol. Databases Curation 2021, baab010 (2021).
86. Medvedeva YA, Lennartsson A, Ehsani R, Kulakovskiy IV, Vorontsov IE, Panahandeh P, Khimulya G, Kasukawa T, FANTOM Consortium, Drabløs F, EpiFactors: a comprehensive database of human epigenetic factors and complexes. Database J. Biol. Databases Curation 2015, bav067 (2015).
87. Marakulina D, Vorontsov IE, Kulakovskiy IV, Lennartsson A, Drabløs F, Medvedeva YA, EpiFactors 2022: expansion and enhancement of a curated database of human epigenetic factors and complexes. Nucleic Acids Res. 51, D564–D570 (2022).
88. Bodenhofer U, Bonatesta E, Horejš-Kainrath C, Hochreiter S, msa: an R package for multiple sequence alignment. Bioinformatics 31, 3997–3999 (2015). [PubMed: 26315911]

89. Charif D, Lobry JR, “SeqinR 1.0–2: A Contributed Package to the R Project for Statistical Computing Devoted to Biological Sequences Retrieval and Analysis” in Structural Approaches to Sequence Evolution: Molecules, Networks, Populations, Bastolla U, Porto M, Roman HE, Vendruscolo M, Eds. (Springer, Berlin, Heidelberg, 2007; 10.1007/978-3-540-35306-5_10)Biological and Medical Physics, Biomedical Engineering, pp. 207–232.

90. Binder JX, Pletscher-Frankild S, Tsafou K, Stolte C, O’Donoghue SI, Schneider R, Jensen LJ, COMPARTMENTS: unification and visualization of protein subcellular localization evidence. Database 2014, bau012 (2014). [PubMed: 24573882]

91. Zeke A, Bastys T, Alexa A, Garai Á, Mészáros B, Kirsch K, Dosztányi Z, Kalinina OV, Reményi A, Systematic discovery of linear binding motifs targeting an ancient protein interaction surface on MAP kinases. Mol. Syst. Biol 11, 837 (2015). [PubMed: 26538579]

92. Metz KS, Deoudes EM, Berginski ME, Jimenez-Ruiz I, Aksoy BA, Hammerbacher J, Gomez SM, Phanstiel DH, Coral: Clear and Customizable Visualization of Human Kinome Data. Cell Syst. 7, 347–350.e1 (2018). [PubMed: 30172842]

93. Wagih O, ggseqlogo: a versatile R package for drawing sequence logos. Bioinformatics 33, 3645–3647 (2017). [PubMed: 29036507]

94. Shepherd MM, ExperimentHub: Client to access ExperimentHub resources. (2023).

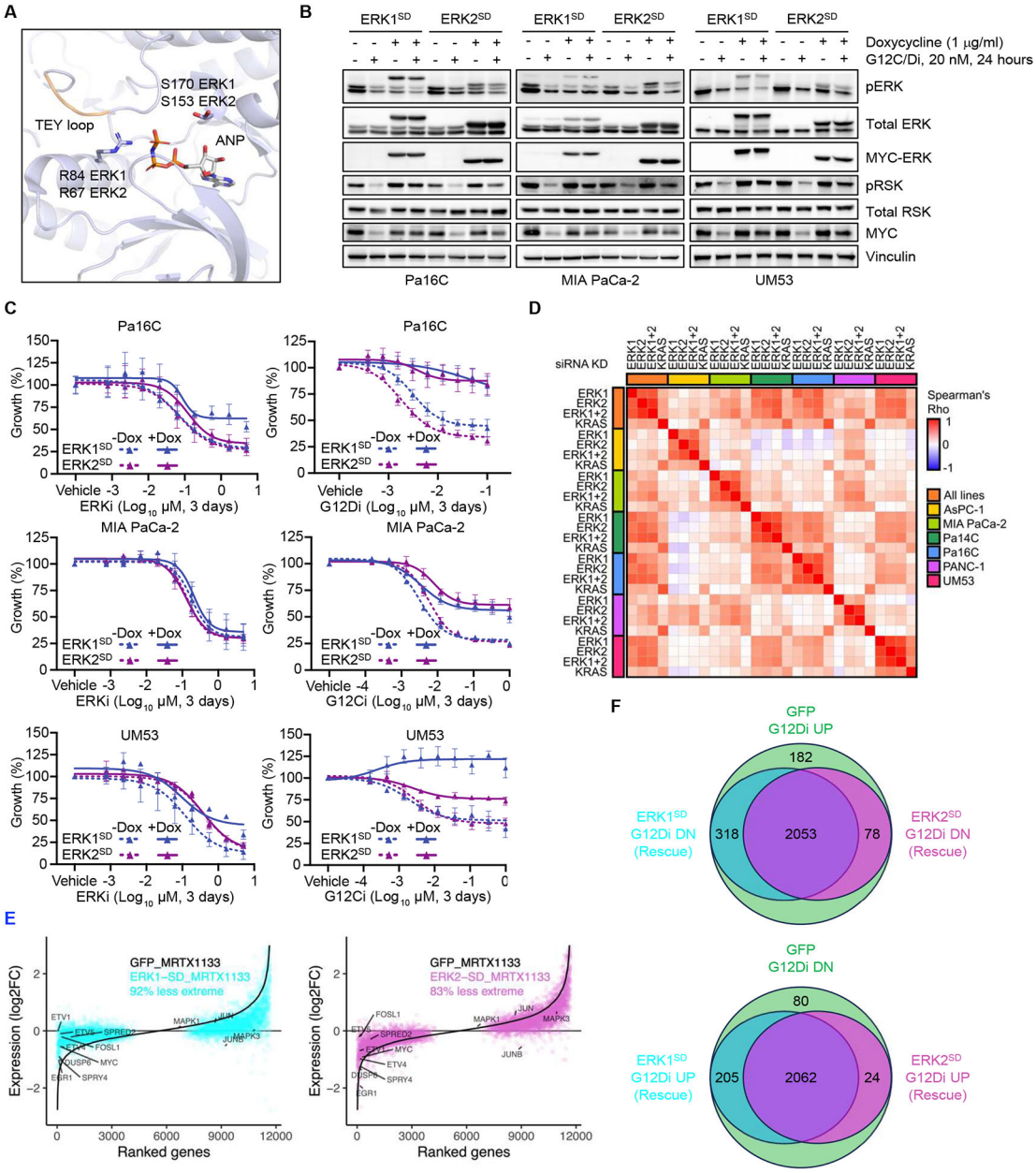

Fig. 1. ERK signaling is critical for KRAS-regulated PDAC growth.

(**A**) Crystal structure of ERK2 bound to the ATP analogue ANP; activating ERK2 mutations (and analogous ERK1 mutations) and the TEY activation loop are shown (PDB: 4NIF). (**B**) Immunoblots showing mutant ERK expression and rescue of downstream signaling in Pa16C, MIA PaCa-2, and UM53 cells with doxycycline (Dox)-inducible activated $ERK1^{SD}$ (R84S/S170D) or $ERK2^{SD}$ (R67S/S153D) treated with the $KRAS^{G12D}$ (MRTX1133, 20 nM) or $KRAS^{G12C}$ (MRTX1257, 20 nM) inhibitor for 24 hours. Dox (1 μg/mL) was added 24 hours prior to drug treatments. Blots are representative of three or more independent experiments. Quantification of pRSK and MYC are shown in fig. S1C. (**C**) Cell viability assays of Pa16C, MIA PaCa-2, UM53 cells with Dox-inducible expression of activated $ERK1^{SD}$ (R84S/S170D) or $ERK2^{SD}$ (R67S/S153D) in response to $KRAS^{G12C/D}$

(MRTX1257, MRTX1133) or ERK1/2 inhibitor (SCH772984). Dox treatment (1 μg/mL) was added 24 hours prior to drug treatments. Graphs show the mean percent growth of three replicates +/− standard error of the mean. (**D**) RPPA Spearman correlation coefficients comparing $\log_2$(FC) of signals from 147 antibodies for the individual six cell lines and all cell lines considered together. Cells were treated with siRNAs targeting NS (non-specific control), *KRAS*, *MAPK3* (ERK1) and/or MAPK1 (ERK2), for 72 hours as in (fig. S1E). Statistical analysis was performed from four biological replicates. The individual treatments and full protein list can be found in fig. S1G and data S1. (**E**) RNA transcript expression changes induced by 24-hour $KRAS^{G12D}$ inhibition (MRTX1133, 100 nM) versus DMSO control in Pa16C cells expressing activated $ERK1^{SD}$ (cyan), $ERK2^{SD}$ (pink), or GFP control (black). Genes are ranked by expression changes in GFP expressing cells. Dox (1 μg/mL) was added 24 hours prior to drug treatments. Statistical analysis was performed from two biological replicates. Genes shown for $ERK1^{SD}$ and $ERK2^{SD}$ (points) are those with significant DE induced by $KRAS^{G12D}$ inhibition in GFP control cells (adj. p-val. < 0.01). (**F**) Venn diagrams representing the overlap between genes upregulated (G12Di UP) or downregulated (G12Di DN) by $KRAS^{G12D}$ inhibition in GFP expressing cells (green; |log2FC| > 0.25 and adj. p-val. < 0.01) and genes rescued by $ERK1^{SD}$ (cyan) and $ERK2^{SD}$ (pink). The center overlap (purple) depicts genes rescued by both $ERK1^{SD}$ and $ERK2^{SD}$, the genes in only the green area are not rescued by either, in the cyan area rescued by only $ERK1^{SD}$, and in the purple area by only $ERK2^{SD}$. The term “rescue” indicates an expression change (log2FC) less extreme than the GFP control but no p-values were used to represent the degree of those expression changes.

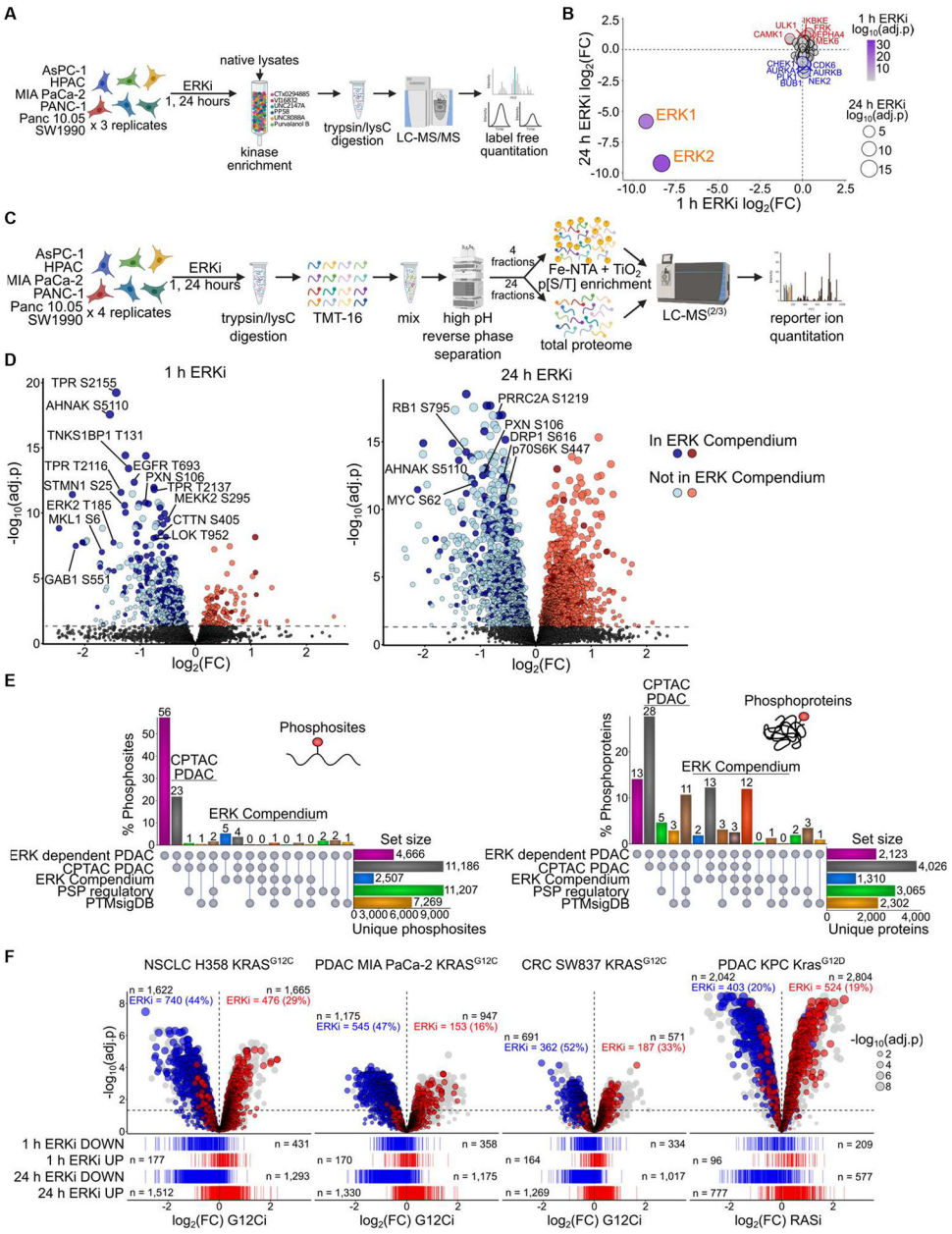

Fig. 2. Phosphoproteomic determination of the ERK regulated phosphoproteome in KRAS mutant PDAC.

(**A**) Flow diagram of the MIB/MS experiment was created with BioRender.com. (**B**) MIB/MS analyses of six KRAS mutant cell lines treated for 1 or 24 hours with ERKi (SCH772984, 1 μM). (**C**) Experimental workflow for proteomics analyses, created with BioRender.com. (**D**) Differentially expressed phosphosites following 1 and 24 hours ERK inhibition in the same six PDAC cell lines as in (A and B). Phosphosites previously reported in the ERK Compendium are highlighted, and top significantly dysregulated sites identified within the ERK Compendium as direct substrates of ERK are labeled. (**E**) Overlap between ERK-dependent phosphosites ($p < 0.05$) or phosphoproteins in PDAC and phosphosites/phosphoproteins reported in the CPTAC PDAC dataset (fdr <

0.05), ERK Compendium, PhosphoSitePlus (PSP) regulatory sites, and Post-Translational Signature Database (PTMsigDB). (**F**) Differentially expressed phosphosites following 24-hour $KRAS^{G12C}$ inhibition (MRTX1257, 20 nM, G12Ci) or RAS(ON) multi-selective tri-complex inhibition (RMC-7977, 10 nM, RASi). ERK-dependent phosphosites ($p<0.05$, 24 h) are annotated by blue (downregulated) or red (upregulated) points. ERK-regulated phosphosites at 1 and 24 hours are annotated as bars below the volcano plot.

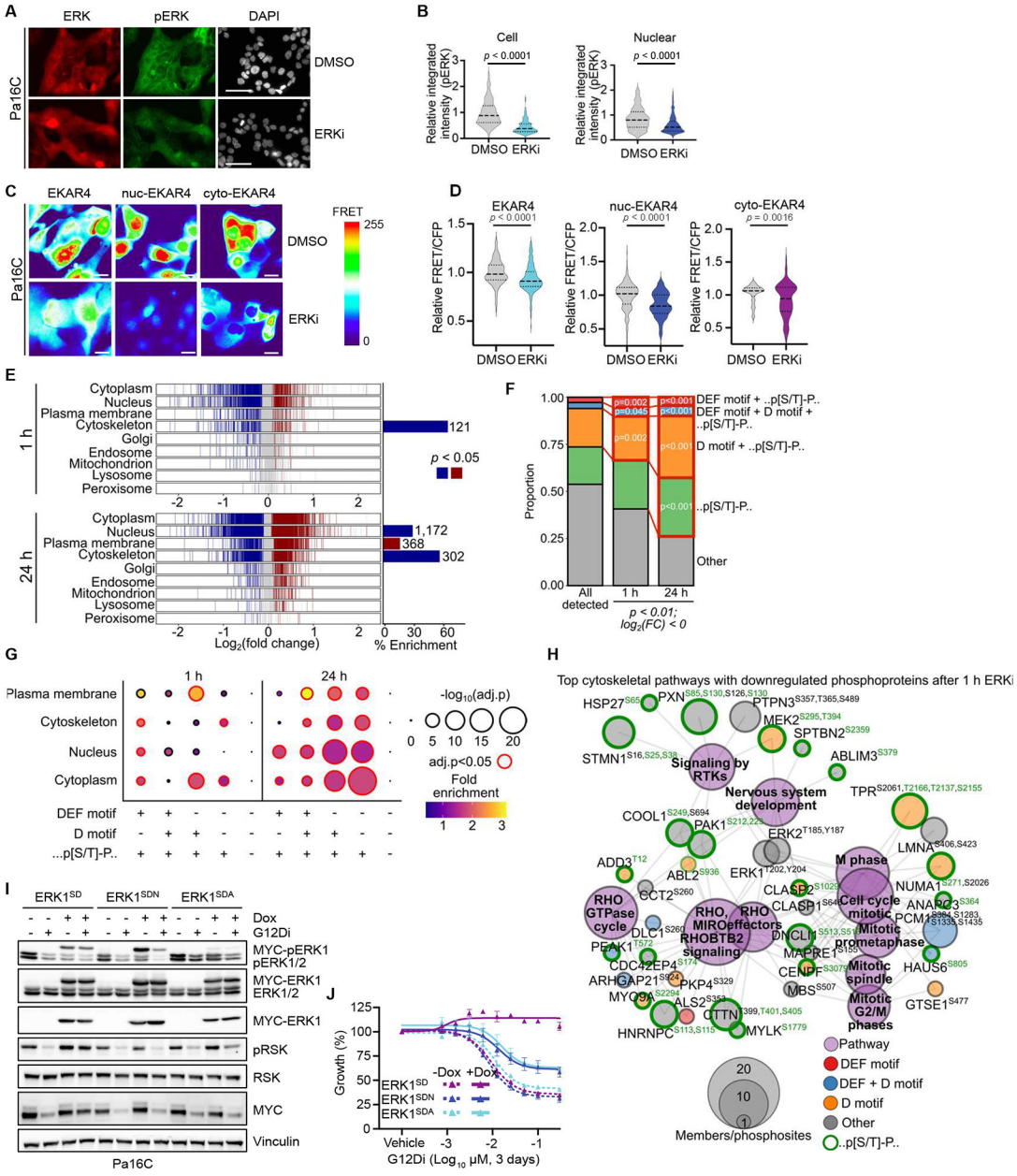

Fig. 3. The ERK phosphoproteome regulates diverse functional pathways comprised of proteins enriched in ERK binding motifs.

(**A**) Representative images of pERK (red), total ERK (green), and nuclear DAPI (grey) immunofluorescence in Pa16C cells treated with ERKi (SCH772984, 1 μM) or DMSO for 24 hours (scale bar = 75 μm), quantified in (**B**) Dashed lines represent median, and statistics represent a Mann-Whitney test on 113–655 individual cells from 5–10 fields of at least two replicates. (**C**) Representative pseudo-colored FRET intensity of Pa16C cells stably expressing untargeted EKAR4 (EKAR4) or EKAR4 tagged with either a nuclear localization signal (nuc-EKAR4) or nuclear export signal (cyto-EKAR4) treated with ERKi (SCH772984, 1 μM) or DMSO for 4 or 24 hours (scale bar = 20 μm), quantified in (**D**). Statistical analysis performed as in (B). (**E**) Subcellular association of phosphoproteins with

differentially regulated phosphosites and enrichment (red/blue, p<0.05) at 1 hour and 24 hours ERKi. Statistical analysis of enrichment determined by one-tailed hypergeometric testing and p values corrected by Benjamini-Hochberg. (**F**) Proportion of phosphosites containing the p[S/T]-P phospho motif together with an ERK-binding D or DEF motif within the phosphoprotein. Proportions were determined within the background of all detected phosphosites, and sites differentially downregulated at 1 hour and 24 hours ERKi ($p < 0.01$, $\log_2(FC)<0$). Statistical analysis of enrichment determined as in (E). (**G**) Subcellular association of phosphoproteins with ERK binding and phosphorylation motifs as in (F). Point color and size represent relative enrichment and significance of enrichment, respectively. Points are highlighted if statistically enriched (red, adj. $p < 0.05$). Enrichment was determined using one-tailed hypergeometric enrichment using all detected phosphosites as background. (**H**) Membership of phosphoproteins within top enriched gene sets for cytoskeleton-associated phosphoproteins with downregulated phosphosites at 1 hour ERKi. Phosphoproteins are colored by the presence of ERK-binding D or DEF motifs and outlined in green if a differentially regulated phosphosite was detected with a p[S/T]-P motif. Size of phosphoproteins is proportional to the number of downregulated phosphosites, and pathways are sized by the number of phosphoprotein members. Differentially regulated phosphosites are also shown and likewise colored green if the phosphosite contains a p[S/T]-P motif. (**I**) Immunoblots showing mutant ERK expression and downstream signaling in Pa16C expressing dox-inducible $ERK1^{SD}$, $ERK1^{SDN}$ (R84S/S170D/D338N), and $ERK1^{SDA}$ (R84S/S170D/Y280A) treated with the $KRAS^{G12D}$ inhibitor (MRTX1133, 20 nM) for 24 hours. Dox (1 μg/mL) was added 24 hours prior to drug treatments. Blots are representative of three or more independent experiments and quantification of pRSK and MYC are in fig. S3Q. **(J)** Viability of Dox-inducible $ERK1^{SD}$, $ERK1^{SDN}$, and $ERK1^{SDA}$ cell lines treated with a dose escalation of G12Di (MRTX1133). Dox (1 μg/mL) was added 24 hours prior to drug treatments. Graphs show the mean percent growth of three replicates +/− standard error of the mean.

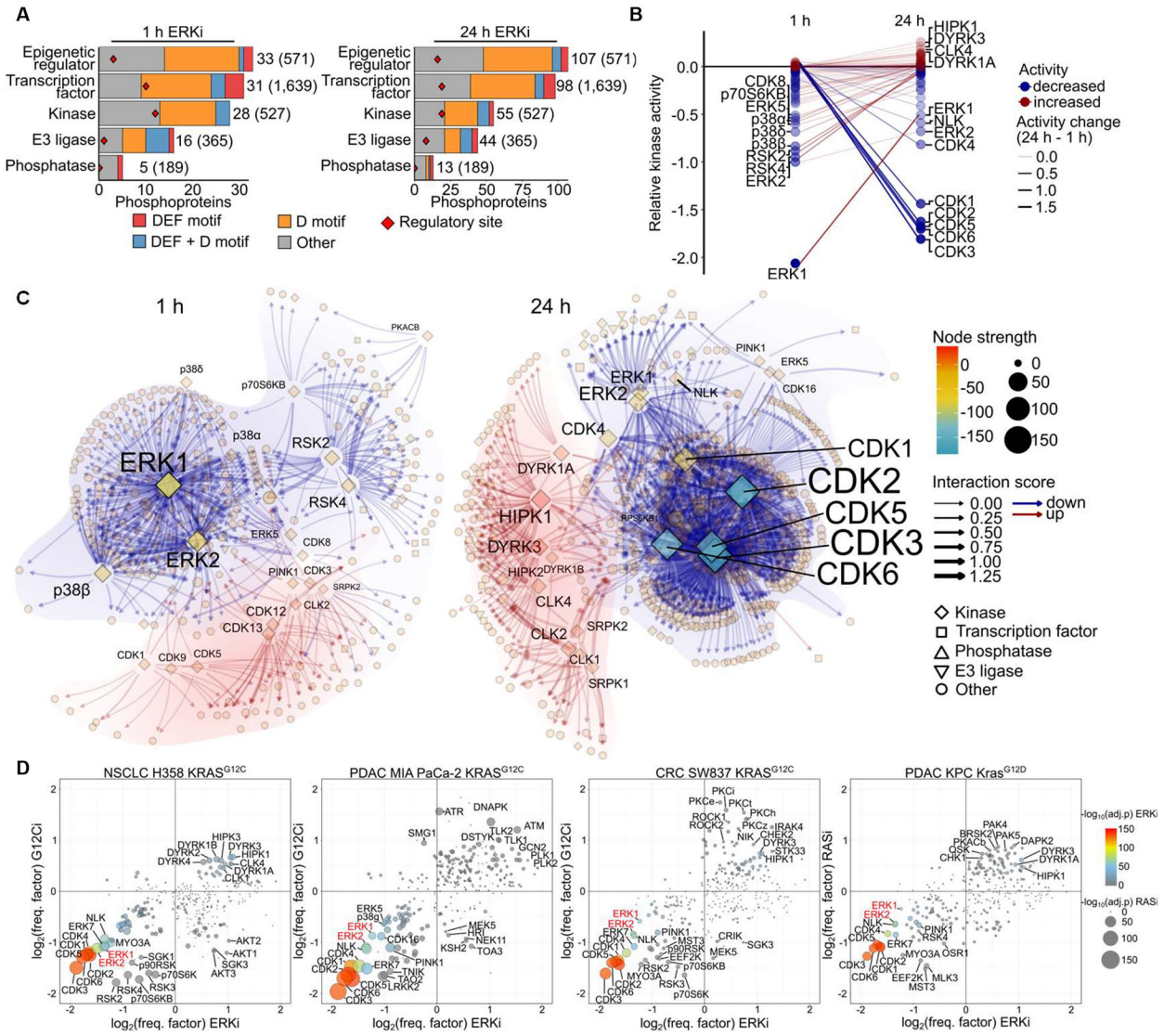

Fig. 4. ERK regulates a dynamic phosphoproteome by engaging downstream kinases.

(**A**) Epigenetic regulator, transcription factor, kinase, phosphatase, and E3 ubiquitin ligase phosphoproteins with downregulated phosphosites and their ERK binding DEF and/or D motifs. The number of phosphoproteins containing a downregulated known regulatory phosphorylation is annotated with a red triangle. (**B**) Relative kinase activities calculated for 303 S/T kinases at 1 hour and 24 hours ERKi using kinase motif specificities (37). Line color represents the direction of change from 1 to 24 hours ERKi, and line transparency represents the magnitude of change. (**C**) Kinase-substrate networks at 1 and 24 hours ERKi. Networks were constructed using kinase motif specificities (37), kinase-substrate specificities from PhosphoSitePlus (25), kinase-substrate interactions from PhosphoNetworks (38) and BioGRID (39). Nodes are sized and colored by their strength in network, and shape represents protein group. Edges are colored by direction of association with up- or downregulated phosphosites. Edge width represents the magnitude of interaction score. The top quantile of kinases is labeled in each network; text size is scaled with node

strength. (**D**) Comparison of kinase-motif enrichment (log_2(freq. factor)) derived from ERK-dependent phosphoproteome versus RAS-dependent phosphoproteomes as shown in Fig 2F. Fill color represents the significance of enrichment in the ERK-dependent phosphoproteome and size represents the significance in the $KRAS^{G12C}$- or RAS-dependent phosphoproteome.

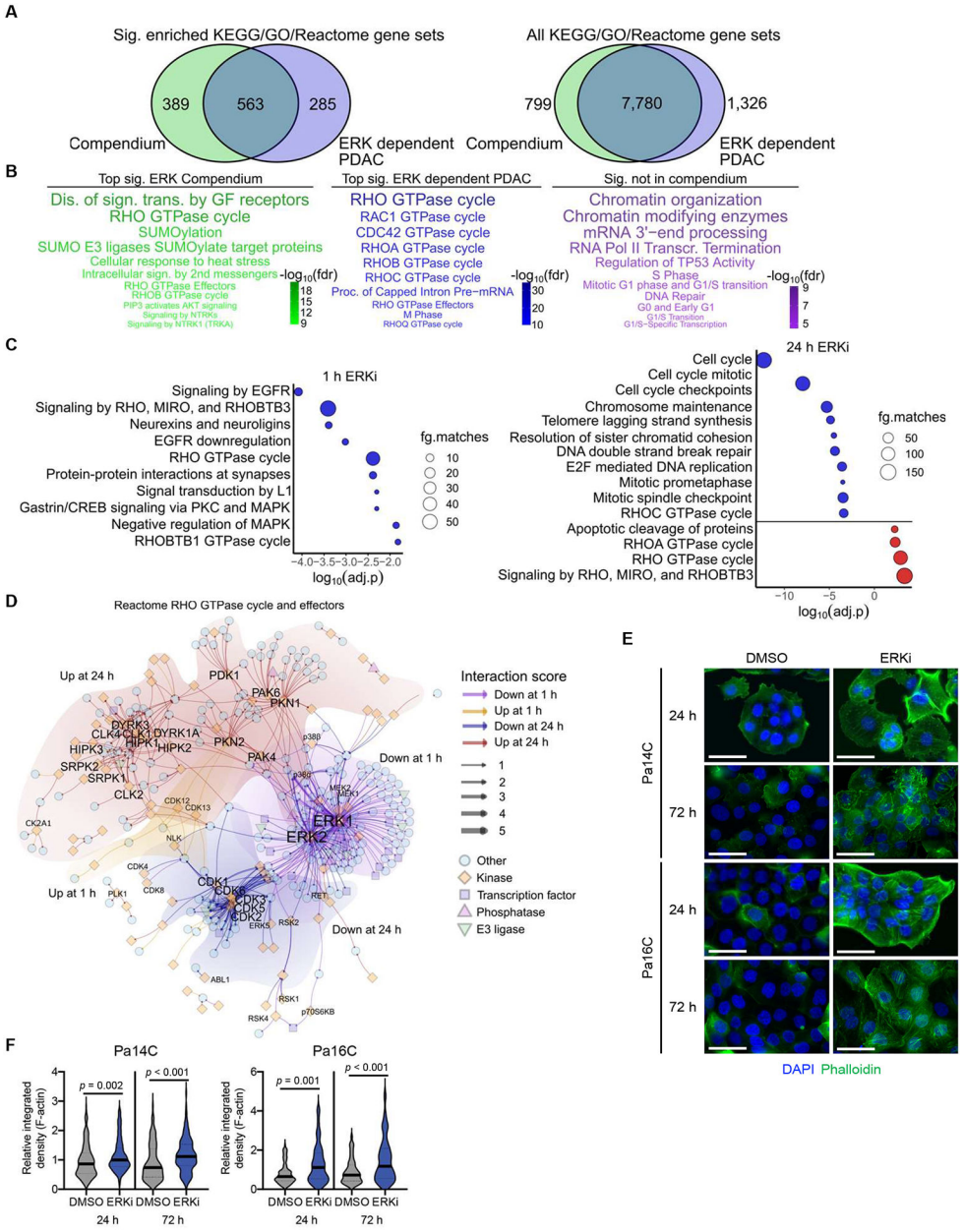

Fig. 5. ERK signaling is highly integrated with RHO GTPase signaling.

(**A**) Overlap of KEGG, Gene Ontology (GO), and Reactome gene sets significantly enriched in ($p < 0.01$, left) or containing any gene associated with (right) phosphoproteins reported in the ERK Compendium (21) or the ERK-dependent PDAC phosphoproteome. Gene set enrichment was determined using one-tailed hypergeometric testing using the entire proteome as background for both phosphoprotein lists; p values corrected by Benjamini-Hochberg. (**B**) Terms of top Reactome gene sets significantly enriched in the ERK Compendium (left), in the ERK dependent PDAC phosphoproteome (middle), or in the ERK dependent PDAC phosphoproteome but not the ERK Compendium (right). Terms are sized and colored by significance of enrichment. (**C**) Signed significance from gene enrichment analysis of up- or downregulated phosphoproteins ($\log_2(FC) < 0$ or > 0; adj. $p < 0.05$) at

1 and 24 hours ERKi. Up- and downregulated phosphoprotein enrichment is represented by fill color (red and blue respectively) with number of phosphoproteins annotated as size by foreground matches. (**D**) Isolated network for edges connecting to proteins within the Reactome “RHO GTPase cycle” and “RHO GTPase effectors” gene sets with interaction scores greater than one standard deviation. Edges are colored by time point (1 or 24 hours) and phosphosite change (up- or downregulated) and edge-node associations are outlined (Down at 1 hour, Down at 24 hours, Up at 1 hour, Up at 24 hours). Top kinases by strength are labeled and node sized by strength. **(E)** Representative images of phalloidin (green) and nuclear DAPI (blue) immunofluorescence in Pa14C and Pa16C cells treated with ERKi (1 μM, SCH772984) or DMSO for 24 hours or 72 hours (scale bar = 50 μm). (**F**) Quantification of relative integrative intensity of F-actin from (E). Solid line represents median, dashed line represents upper and lower quartiles, and statistics represent a Mann-Whitney test on 113–655 individual cells from 5–10 fields of at least two replicates.

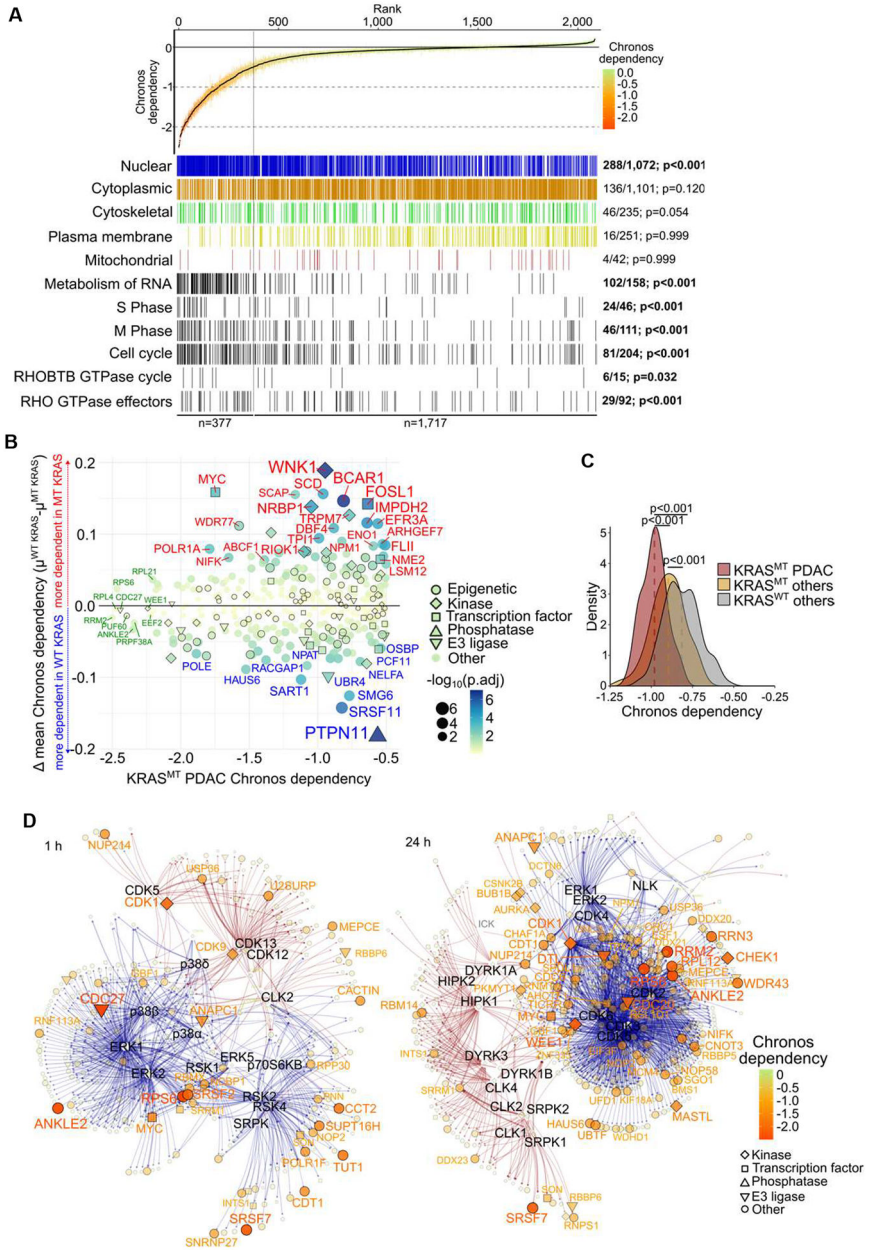

Fig. 6. Genetic dependencies of the ERK dependent PDAC phosphoproteome.

(**A**) Annotated Chronos dependency rank plot, ranked by DepMap dependency scores for ERK-regulated phosphoproteins. Median Chronos dependency across 43 KRAS MT PDAC cell lines for each phosphoprotein is represented as a point on the rank plot. The line for each point represents upper and lower quartiles and is colored by the median dependency. Annotations indicate membership in the subcellular compartment or Reactome gene set. Enrichment significance was determined by one-tailed hypergeometric testing of phosphoproteins with median Chronos scores < −0.5 (dotted line); *p* values corrected by Benjamini-Hochberg. (**B**) Selectivity of genetic dependencies for ERK regulated phosphoproteins towards KRAS MT or KRAS WT cancers. Cell lines from cancers of the pancreas, large intestine, biliary tract, lung, stomach, endometrium, cervix, or ovary were

characterized as either KRAS mutant, including G12A/C/D/R/S/V, G13D, or Q61K/H/L/R mutations, or KRAS WT. The mean difference in Chronos dependency (y-axis) in KRAS MT and KRAS WT cell lines is shown for each ERK-regulated phosphoprotein with respect to the mean Chronos dependency in KRAS MT PDAC (x-axis). Genes are colored and sized by adjusted p values calculated by two-way ANOVA and Tukey's HSD post hoc test between KRAS MT and KRAS WT cell lines, with cancer type as an independent variable. (**C**) Density histogram of mean genetic dependencies of the 23 genes with significantly selective dependencies in KRAS MT cancers as shown in (B), separated by KRAS MT PDAC versus other cancers from (B) defined as KRAS MT or KRAS WT. Statistical differences determined by Games-Howell. (**D**) Kinase-substrate network from 1 and 24 hours ERKi treatments with node size and color representing median genetic dependency of the 43 KRAS MT PDAC cell lines. Edges represent interaction scores as in Fig. 4C.